Annual Review of Fluid Mechanics

Aircraft Icing: Modeling and Simulation

Alberto Guardone,[1] Tommaso Bellosta,[1] Alessandro Donizetti,[1] and Mariachiara Gallia[2]

[1]Department of Aerospace Science and Technology, Politecnico di Milano, Milano, Italy; email: alberto.guardone@polimi.it

[2]Institut für Strömungsmechanik, Technische Universität Braunschweig, Braunschweig, Germany

Annu. Rev. Fluid Mech. 2026. 58:139–65

First published as a Review in Advance on September 18, 2025

The *Annual Review of Fluid Mechanics* is online at fluid.annualreviews.org

https://doi.org/10.1146/annurev-fluid-112723-062537

Keywords

in-flight icing, multiphase flows, droplet dynamics, phase change, film dynamics, flow simulation, aircraft certification

Abstract

In-flight ice accretion poses a major safety concern in aviation. It occurs due to the icing from clouds of supercooled water droplets, the accumulation of ice crystals at high altitudes, or snow buildup. Assessing the detrimental effects of ice accretion on aircraft performance and handling qualities is a complex, multidisciplinary task, as it requires modeling the dynamics of the dispersed phase (water droplets, ice crystals, and snowflakes), the particle impact dynamics and its interaction with the aircraft surfaces, the liquid film dynamics, the solidification process, and possibly ice shedding. The ice protection systems must also be modeled. The present review addresses the status of ice accretion models and simulation tools. The intrinsically stochastic nature of ice accretion, combined with substantial operational and modeling uncertainties, makes it challenging to validate these tools against experimental observations and use simulation as a reliable means of compliance for certification in icing conditions, especially for innovative aircraft configurations such as wing-body and advanced urban air mobility vehicles.

1. INTRODUCTION

Supercooled large droplets (SLDs): defined by the World Meteorological Organization as supercooled droplets larger than 50 μm; encompass freezing drizzle and freezing rain

Anti-ice mode: mode in which ice accretion on the surface is avoided by continuously operating the system

De-ice mode: mode in which the already formed layer of ice is removed with cyclic operation

Supplemental Material >

In-flight liquid icing occurs when an aircraft flies through clouds of supercooled droplets, specifically, liquid water drops that are below freezing temperature and freeze upon impact on the aircraft surface, leading to three characteristic ice types. Rime ice forms at low temperatures when supercooled droplets freeze on impact into opaque, air-entrained, rough ice accretion. Glaze ice appears at higher temperatures and at higher liquid water content (LWC), as a thin film of water spreads before freezing into clear, smoother ice often bearing horn-like structures. Mixed ice results from a transition between these two regimes, combining characteristics of both rime and glaze. Ice accretion roughens the surface, disturbs the boundary layer, reduces lift and thrust, increases drag, obstructs sensors and probes, and, in extreme cases, can lead to engine failure or loss of control. The European Union Aviation Safety Agency (EASA) has classified in-flight icing—whether from supercooled droplets, supercooled large droplets (SLDs), ice crystals, or snow—as a top safety priority for large transport aircraft, reflecting its potential to compromise performance margins and airworthiness (Cebeci & Kafyeke 2003). To prevent, delay, or remove ice accretion on the surface, ice protection systems (IPSs) are used in either anti-ice mode or de-ice mode. Trains, civil structures, cables, ships, and wind turbines operating in cold environments are susceptible to ice accretion and can benefit from the scientific knowledge and numerical technologies developed in aviation.

Understanding in-flight icing requires understanding of the fluid mechanics of the atmosphere; aircraft aerodynamics; the dynamics of dispersed phases such as water droplets, ice crystals, and snowflakes (Balachandar & Eaton 2010); particle impact dynamics and their interaction with aircraft surfaces (Yarin 2006); liquid film dynamics; and the solidification process (Huerre et al. 2025). Heat transfer from solid surfaces, the liquid film, and the external aerodynamic field significantly influences ice accretion and the operation of active IPSs relying on thermal (Mohseni & Amirfazli 2013), mechanical (Budinger et al. 2021), or chemical systems (Kozomara et al. 2023). Active IPSs can be utilized in combination or replaced by passive IPSs employing icephobic or hydrophobic coatings, further increasing the complexity of the ice/water film interaction with these engineered surfaces. Additional references on IPSs are provided in the **Supplemental Appendix**. Due to the lengthy accretion times required by regulations, substantial ice formations may develop, significantly impacting the aircraft aerodynamics. The icing process is greatly influenced by atmospheric and flight parameters outlined in the sidebar titled Icing Parameters.

ICING PARAMETERS

Environmental Parameters

The environmental parameters that identify icing conditions include the ambient temperature T, pressure P, liquid water content (LWC), median volume diameter (MVD), and droplet size distribution. The LWC is the mass of water contained in a unit volume of air, measured in grams per cubic meter. The MVD denotes the median diameter value of the droplets in the cloud.

Flight Parameters

The most relevant parameter is the aircraft speed v_∞, which directly influences the stagnation temperature at the aircraft surface. The flight configuration (attitude, deployment of the aerodynamic surfaces, engine operation, and operation of the IPS) also impacts the amount of impinging water, its distribution on the aircraft, and the icing process.

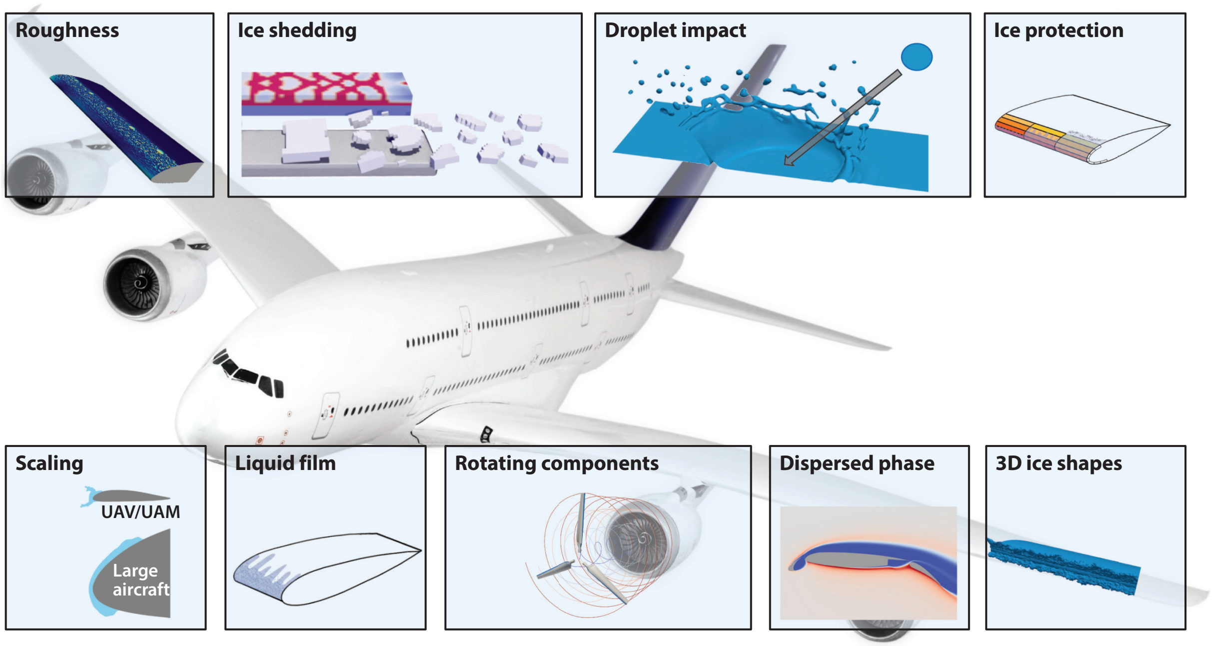

Figure 1

Schematics of the physics of in-flight ice accretion. Abbreviations: UAM, urban air mobility; UAV, uncrewed aerial vehicle. Ice shedding image reproduced with permission from Nezzar et al. (2024).

Figure 1 highlights the diverse fluid dynamics problems related to ice accretion and provides a map to navigate this article. In particular, open questions in icing research concern the modeling of surface roughness and its influence on aircraft aerodynamics and heat transfer; the modeling and simulation of ice shedding resulting from aerodynamic or centrifugal forces or from the operation of the IPS; the modeling of particle interaction with the aircraft surface, particularly concerning engineered surfaces; the design and operation of different types of IPSs; the prediction of complex 3D ice shapes and their impact on aerodynamic performance; the dynamics of the dispersed phase, specifically for SLDs, ice crystals, and snow; ice accretion on rotating components such as jet engine fans, large propeller or open-rotor configurations, helicopter rotors, and drones; liquid film dynamics and the formation of rivulets and liquid film shedding; and the increased severity of the ice encounter for smaller aircraft, which is relevant for operating advanced urban air mobility (AUAM) and uncrewed aerial vehicles (UAVs) in icing conditions.

2. MODELING AND SIMULATION OF IN-FLIGHT ICING

Figure 2 illustrates a simplified representation of an aircraft flying into a quiescent mixture of air and water droplets. Using a reference length l of 1 m, such as the mean aerodynamic chord of a small aircraft, and a reference speed v_∞ of 100 m/s results in a Reynolds number of approximately 10^6. The flow Reynolds number associated with icing can vary from approximately 10^7 for large commercial jets to 10^5 for smaller aircraft and drones.

Certification requirements and early experimental measurements (Hess et al. 1998, Rosenfeld & Lensky 1998) for liquid ice accretion indicate that icing clouds typically have droplet diameters d ranging from 10 to 100 μm, with maximum values reaching up to 1,000 μm, and an LWC of the order of 1 g/m^3, yielding a volume fraction of the dispersed phase of $\sim 10^{-6}$. This low-volume

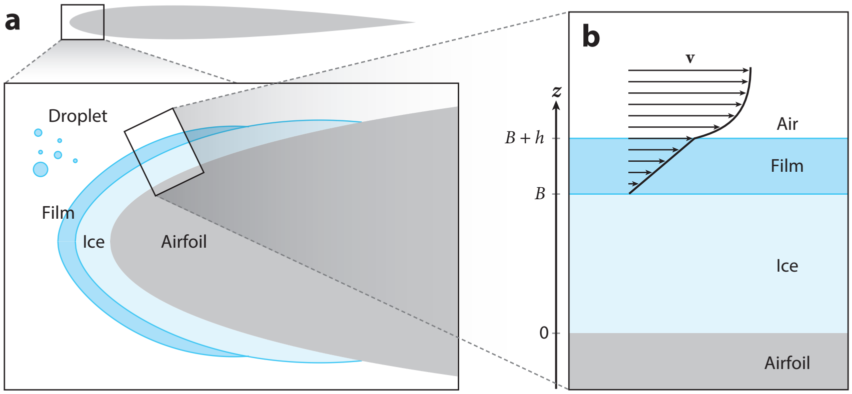

Figure 2

(*a*) Representation of the multiphase icing problem. (*b*) Definition of the local reference system in Equation 3.

fraction allows the introduction of the one-way coupling hypothesis for the dispersed phase. Under these conditions, the Stokes number, which relates the relaxation time of a particle governed by the Stokes drag law to the aerodynamic timescale defined as $t_f = l/v_\infty$, can be of the order of unity or lower. At the surface, a cold substrate is in contact with a growing ice layer, possibly covered by a liquid film or directly in contact with air, as in **Figure 2**. Neglecting thermal deformation, the evolution of the substrate and ice layers is governed by the heat equation, and the liquid film dynamics is described by the heat equation coupled with the incompressible Navier–Stokes equations. The dispersed-phase flow, liquid film, ice layer, and heat transfer at the solid substrate are coupled via boundary conditions at the corresponding interfaces. At the air–film interface, mass is exchanged due to the impingement of water droplets. The continuity of the temperature T and of the heat flux $k\nabla T$, where k is the thermal conductivity, is enforced at the air–film and ice–substrate interfaces. At the ice–water interface, the temperature is equal to the freezing temperature of water, while the interface velocity is determined by the net heat flux at the interface. Representative values of the thickness of ice and film in aircraft icing are $\mathcal{O}(10^{-2})$ m and $\mathcal{O}(10^{-4})$ m, respectively.

Stokes number: the ratio of the characteristic time of the particle to a characteristic time of the flow $\mathrm{St} = \frac{t_p v_f}{l}$, where t_p is the relaxation time of the particle, v_f is the characteristic fluid velocity, and l is the characteristic flow dimension

Collection efficiency (β): the ratio of the mass flux of the water impinging on the surface over the free-stream water mass flux

Quasi-steady approximation: in steady flows, the timescale for ice accretion is larger than that of aerodynamics and the dispersed phase; the three physical problems are solved using a loosely coupled, segregated approach

Ice accretion affects aircraft performance within minutes of the onset of the ice encounter. To estimate the icing timescale, the reference velocity is defined as the freezing rate in rime conditions, namely $v_{ice} = \dot{m}_{imp}/\rho_i = \beta\, v_\infty\, \mathrm{LWC}/\rho_i$, over a reference length, where $\dot{m}_{imp}$ is the impinging water mass flux per unit time and area and β is the collection efficiency. Considering typical values for in-flight icing, we find $t_{ice}/t_f = \rho_{ice}/(\beta\, \mathrm{LWC}) \approx 10^6 \gg 1$. In the following, the subscripts i and w indicate ice and water properties, respectively, such as the ice density ρ_i. The subscript ice is reserved for quantities describing the ice accretion process, such as the ice front velocity v_{ice} or the mass of ice accreted per unit time and area $\dot{m}_{ice}$.

Thanks to the scale separation, the unsteady accretion process can be represented as a series of quasi-steady states. Based on the quasi-steady assumption and the small volume fraction of particles, airflow is initially calculated around the clean geometry. Subsequently, the water that accumulates on the aircraft surfaces is estimated by simulating the evolution of the dispersed phase. A thermodynamic solver finally determines the ice growth rate over the surface grid, leading to the formation of an ice layer. A liquid film model is included when necessary. The criteria for ice shedding are also checked. A new computational mesh is obtained for the iced configuration, and the whole process is repeated.

Under the quasi-steady approximation, the total ice accretion time is divided into smaller steps. This so-called multistepping approach aims to account for the feedback of the growing ice on the

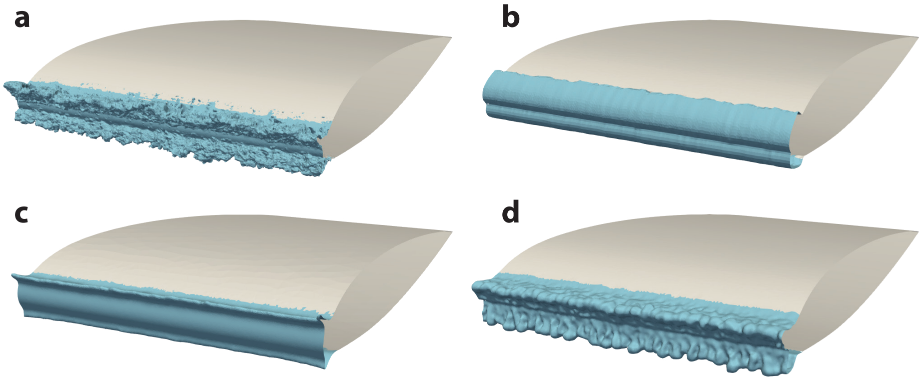

Figure 3

(*a*) Experimental ice shape from case 242 of the 1st AIAA Ice Prediction Workshop. Image created using data from Laurendeau et al. (2022). (*b*) Single-step Messinger. (*c*) Multistep Messinger. (*d*) Multistep morphogenetic.

aerodynamics and droplet dynamics. The number of steps used ranges from one (single step) to approximately 10 steps for large 3D simulations (and even more for 2D simulations), depending on the ice type and exposure time. Rime ice generally needs fewer steps than glaze due to a smaller influence on the aerodynamics (Ozcer et al. 2022). The number of steps can be selected based on best practices or automatically from numerical stability concerns (Donizetti et al. 2024a). As shown in **Figure 3**, single-step runs (**Figure 3*b***) cannot represent the glaze ice horns seen in the experiments in **Figure 3*a***, whereas multistep simulations (**Figure 3*c*,*d***) can predict features stemming from the coupling of ice growth, aerodynamic, and dispersed-phase solutions. The predictor–corrector approach of Radenac et al. (2023) aims to retain the computational efficiency of single-shot methods (a predictor step) while enhancing prediction through a corrector step. The correction involves computing the evolution of the ice thickness, using a blend of solutions derived from the clean configuration and predictions made by the single-shot approach as boundary conditions for the thermodynamic problem. Aliaga et al. (2011) pioneered a fully unsteady approach in which the aerodynamics and dispersed phase are solved as a coupled system. Surface energy and mass balances are considered in a segregated manner. This review specifically focuses on liquid icing simulations. Readers are encouraged to refer to the recent work of Peters et al. (2024) for in-flight icing caused by ice crystals and of Aguilar et al. (2023) for snow.

2.1. Aerodynamics

The evaluation of the aerodynamic field around the aircraft is the first step in a typical icing simulation, as it determines the dynamics of the dispersed phase and provides the temperature and pressure at the air/liquid film/ice interface, along with shear stresses and heat fluxes, which drive the liquid film dynamics and the ice accretion. Minor errors in the computation of the surface temperature, particularly the stagnation temperature, may affect the accurate identification of the type of ice (rime, glaze, mixed) and the evolution of the ice process, especially regarding glaze ice, which occurs at temperatures relatively close to 0°C.

State-of-the-art ice accretion codes (Beaugendre et al. 2003a, Wright et al. 2008, Radenac et al. 2023, Donizetti et al. 2024b) generally rely on solving the Reynolds-averaged Navier–Stokes (RANS) equations on body-fitted meshes, leveraging their widespread use in industrial settings and the ease of coupling various flow solvers. The immersed boundary method (IBM) offers a viable alternative to body-fitted meshes for representing complex geometries, such as 3D ice shapes (Pena et al. 2016, De Rosa et al. 2023, Paz et al. 2024). A major drawback of the IBM is its requirement to rebuild the external ice surface prior to addressing the thermodynamic step. Glaze ice conditions are extremely sensitive to convective heat transfer coefficient (HTC) distribution, as convective heat transfer at the water surface plays a major role in the energy balance equation. For RANS-based icing approaches, the HTC can be derived from a wall function using a Reynolds-like analogy, two isothermal simulations, or from the computed wall heat flux and a reference temperature (Lavoie et al. 2018). The reference temperature is either the adiabatic recovery temperature or the temperature value sampled at a specific wall distance in viscous units y^+ above the surface.

Heat transfer coefficient (HTC): the amount of convective heat transferred per unit area per unit time, for a given temperature difference between the surface and the fluid

Impinging mass flux ($\dot{m}_{\text{imp}}$): computed per unit area from the aircraft velocity, the LWC, and β as $\dot{m}_{\text{imp}} = v_\infty \text{LWC}\beta$

The use of scale-resolving simulations for in-flight icing prediction remains a relatively unexplored area at the time of writing, largely due to the high Reynolds number of the flow of interest and the significant timescale difference between the resolved turbulent flow features and the ice growth rate. Large eddy simulation (LES) approaches such as hybrid RANS–LES approaches (Costes & Moens 2019), wall-modeled LES (WMLES) (Bornhoft et al. 2024a), and very large eddy simulations (König et al. 2015) have been successfully employed to assess the aerodynamic penalties of ice shapes that arise from properly resolving the large scales more relevant in separated flows. WMLES have been proven to be especially suited to simulate complex 3D iced configurations when solved on body-fitted unstructured Voronoi grids (Bornhoft et al. 2024b) or on immersed-boundary Cartesian grids (Penner et al. 2024, Wong et al. 2024). LES have also been recently employed to predict the heat flux distribution on surfaces contaminated by ice-grown roughness either considering the heat conduction problem in the ice layer (Zabaleta et al. 2024a) or using an isothermal boundary condition at the ice surface (Sotomayor-Zakharov et al. 2025). The effects of icing roughness have been examined on a flat plate through direct numerical simulation, WMLES, and RANS by Hu et al. (2024).

2.2. Particle Dynamics

The simulation of dispersed-phase flows, i.e., of particle dynamics, aims to compute the interaction of the particle cloud with the aircraft. The gas phase is indicated by the subscript f; particles are indicated with p to include droplets, snow, and ice crystals. The quantity of interest from the dispersed-phase model is the impinging mass flux, usually expressed in terms of the collection efficiency β and the LWC.

The liquid phase is dispersed in droplets of a diameter ranging from a few micrometers to hundreds of micrometers. The direct simulation accounting for all scales is, as of now, unfeasible due to the high Reynolds number of the external aerodynamics problems of interest and the number of resolved droplets required to obtain statistical convergence of the collection efficiency. State-of-the-art direct numerical simulations of resolved particles are still limited to much lower Reynolds numbers and canonical flows (see, e.g., Elghobashi 2019).

2.2.1. Governing equations and scaling.

Nondimensional analysis helps simplify the dispersed-phase problem. The diameter of the droplet d is very small relative to the characteristic size l of the steady aerodynamic problem, and hence, a point particle approximation can be employed. The particle Stokes number St, relating the particle response time to the characteristic time of the aerodynamic flow, is $\text{St} = \mathcal{O}(10^{-2})$–$\mathcal{O}(1)$. Considering now the small viscous scales at the wall of characteristic size $l_\nu = \nu/u_\tau$, the condition for point particle approximation is no longer met since the particle diameter expressed in wall units $d^+ = d/l_\nu$ ranges between order 1 and 10. The order of magnitude of the ratio of the particle relaxation time to the viscous timescale is $\text{St}^+ = \mathcal{O}(10^2)$–$\mathcal{O}(10^4)$, which indicates that droplet trajectories are weakly disturbed by the viscous scales at the wall. Brandt & Coletti (2022) provide a detailed description of particle-laden turbulence. The small size of droplets compared to the reference problem length and the characteristic volume fractions of the droplets allow a one-way coupling approach between the dispersed phase and the air as introduced in the seminal work of Elghobashi (1994).

Neglecting phase change and temperature differences, momentum transfer couples the dispersed phase to the continuous (gas) phase. When particles are not resolved, the momentum transfer is modeled using the Basset–Boussinesq–Oseen equation, which separates the forces acting on a rigid sphere at low particle Reynolds numbers $\mathrm{Re_p}$ into the effects of drag, lift, added mass, pressure gradient, Basset history terms, buoyancy, and gravity. Since $\rho_\mathrm{p}/\rho_\mathrm{f} = 10^3 \gg 1$ for the water/air case of interest here, drag and gravity forces dominate the momentum transfer (Maxey & Riley 1983). The equation of motion of a particle made nondimensional using the aerodynamic problem reference length and velocity reads

$$\frac{\mathrm{d}\mathbf{v}_\mathrm{p}}{\mathrm{d}t} = f(\mathrm{Re_p}, \mathrm{We_p})\frac{\mathbf{v}_\mathrm{f} - \mathbf{v}_\mathrm{p}}{\mathrm{St}} + \hat{\boldsymbol{z}}\frac{1}{\mathrm{Fr}^2}, \qquad 1.$$

where the term $f(\mathrm{Re_p}, \mathrm{We_p}) = \frac{\mathrm{Re_p}}{24} C_D$ accounts for deviations of the drag coefficient from that of a rigid sphere in a Stokes flow. For the problem at hand, those deviations are due to finite values of the particle Reynolds number $\mathrm{Re_p}$ and the particle Weber number $\mathrm{We_p}$, which account for changes in the particle geometry. The ratio of the Stokes number St to the square of the Froude number $\mathrm{Fr} = v_\infty/\sqrt{gl}$ is proportional to the ratio of the particle terminal velocity to the freestream velocity for a particle subject to the Stokes drag law. Substituting the parameters typical of in-flight icing, we find $\mathrm{St}/\mathrm{Fr}^2 = \mathcal{O}(10^{-5})$–$\mathcal{O}(10^{-3})$: Particle trajectories are driven by the large gradients in the mean aerodynamic flow, and the effects of gravity can be neglected at least for the smaller droplets.

Diverse first- and second-order effects determine the dynamics of the dispersed phase. In this context, first-order effects are associated with physical phenomena that have a major effect on water collection. Second-order effects contribute negligibly to the collection efficiency when compared to first-order effects. The most significant first-order effects on the collection efficiency are the drag force acting on the particle and the outcome of the particle impingement. Particle drag models usually include effects of finite particle Reynolds numbers and possibly particle shape parameters for SLDs, snow, and ice crystal particles. Numerous drag coefficient formulations for liquid water droplets are available in the scientific literature obtained by fitting experimental data [see, e.g., the model of Schiller (1933), valid up to $\mathrm{Re_p} < 10^3$]. One effect of finite $\mathrm{Re_p}$ values is that the collection efficiency becomes more dependent on the flow Reynolds number, which increases as the Reynolds number decreases for a fixed Stokes number (Wessel & Righi 1988).

The larger inertia of SLDs can lead to larger particle slip velocities $\mathbf{v_r}$ and, hence, Reynolds and Weber numbers. This can cause these particles to significantly deform from their initial spherical shape, altering the drag coefficient and necessitating specific modeling of SLDs in icing codes. The deformation of SLDs can result in aerodynamic breakup (Vargas & Feo 2011). For our reference problem, the particle Weber number $\mathrm{We_p}$ computed using the air density and the freestream velocity as an upper bound for the velocity slip ranges between $\mathcal{O}(1)$ and $\mathcal{O}(10)$. In icing computations, the particle Weber number computed using the local velocity slip is usually employed in aerobreakup models, with a threshold value of $\mathrm{We_p} = 13$ (Wright & Potapczuk 2004). Droplets can deform prior to breaking up at the threshold value of $\mathrm{We_p}$, leading to a modification of the drag coefficient. Droplet deformation can be taken into account by blending the drag model of a sphere with that of a disk as a function of the particle Weber number (Honsek & Habashi 2006).

The particle–wall interaction mechanism also has a significant first-order effect. Yarin (2006) describes different outcomes for droplet–surface interaction such as deposition, spreading, bouncing, and splashing. Nondimensional groups governing the deposition–splashing transition

Particle Reynolds number: represents the ratio of inertial to viscous forces within a fluid flow in the reference frame of the particle and is defined as $\mathrm{Re_p} = \frac{\rho v_\mathrm{r} d}{\mu}$, where ρ, v_r, and μ are reference values of the fluid density, particle slip velocity, and dynamic viscosity and d is the particle diameter

Stokes flow: if $\mathrm{Re_p} \ll 1$, the particle drag coefficient is inversely proportional to the particle Reynolds number; the characteristic time of the particle is $t_\mathrm{p} = \frac{\rho_\mathrm{p} d^2}{18\mu_\mathrm{f}}$

Weber number: proportional to the ratio of inertial to surface tension forces, $\mathrm{We} = \frac{\rho v^2 l}{\sigma}$, where ρ, v, and σ are reference values of the fluid density, velocity, and surface tension and l is the reference dimension

Particle slip velocity ($\mathbf{v_r}$): the difference between the fluid velocity $\mathbf{v}_\mathrm{f}$ and the particle velocity $\mathbf{v}_\mathrm{p}$, $\mathbf{v}_\mathrm{r} = \mathbf{v}_\mathrm{f} - \mathbf{v}_\mathrm{p}$

are available in the literature as a combination of Ohnesorge and Weber (or Reynolds) numbers computed using the droplet properties and the normal impact velocity (Mundo et al. 1995, Cossali et al. 1997). Wright (2006) and Trontin & Villedieu (2017) suggested the most widely employed models for computing the ratio of deposited mass to total impinging mass in icing computations. The models relate the sticking efficiency of the droplets to the Cossali or Mundo parameters when the impingement is almost normal to the surface. At higher impingement angles (i.e., the angle between the particle velocity and the surface normal), the deposited mass depends on the droplet impinging angle. Nonliquid particles experience different wall interaction mechanisms. For example, in ice crystal icing, the impingement behavior is governed by the counteracting effects of sticking and erosion (Trontin & Villedieu 2018, Yang et al. 2023).

Ohnesorge number: proportional to the ratio of viscous to surface tension forces; defined as $\mathrm{Oh} = \frac{\mu}{\sqrt{\rho \sigma d}}$, where μ, ρ, and σ are the viscosity, density, and surface tension and d is a characteristic dimension, typically the droplet diameter

Routine simulations of ice accretion often overlook higher-order effects on the collection efficiency. For example, Saffman and Magnus lift or Basset history forces are usually neglected without affecting the quality of the results. The effect of gravity can have some small influence on SLD dynamics and is generally included only for such particles. Aerodynamic breakup may occur if the local value of the particle Weber number is increased, typically for SLDs in large velocity gradient zones such as near the leading edge of airfoils or in rotating geometries, e.g., propellers or engine fans (Wright & Potapczuk 2004, Bae & Yee 2022). Turbulent diffusion of droplets usually has a negligible influence on the collection efficiency and is thus disregarded in most icing simulations, due to the laminar inflow considered in computations and the high value of St^+ at the viscous walls (Brandt & Coletti 2022). Lee & Loth (2008) showed limited effects on the resulting ice shape when turbulent diffusion is accounted for by employing discrete random walk (DRW) and continuous random walk (CRW) eddy interaction models (Bocksell & Loth 2001). Such eddy interaction models helped predict droplet dispersion in icing wind tunnels and thus the LWC distribution in the test section (Bhargava et al. 2005). Zhang et al. (2025) showed good LWC distribution prediction by employing scale-resolving LESs of the flow around the droplet injectors in an icing wind tunnel, together with a DRW model for the effects of subgrid scales on particle dispersion. Zabaleta et al. (2024b) computed the collection efficiency from a WMLES flow field, thus accounting for the turbulent dispersion of particles caused by the resolved flow scales. Recently, the development and certification of icing wind tunnels for SLD conditions prompted the investigation into the thermal and velocity slip between the droplets and the surrounding flow (Ferschitz et al. 2017). Accounting for thermal and mechanical nonequilibrium at the droplet injection point can be relevant for numerically reproducing SLD wind tunnel measurements (Bora et al. 2023).

2.2.2. Numerical solution of the dispersed-phase model. Either an Eulerian–Lagrangian or an Eulerian–Eulerian representation can be used to describe the particle-laden flow. Both formulations employ the point–particle approximation, either explicitly or implicitly (Balachandar & Eaton 2010). In the Lagrangian description, the particles move as point-wise bodies within an underlying flow field computed using an Eulerian approach. First- and second-order effects, described in the previous section, are accounted for straightforwardly during the computation of particle dynamics integrating Equation 1. The Lagrangian approach requires a relatively large number of particles, especially in 3D simulations, and results might depend on the initial seeding, namely, the cloud definition. Earlier codes employing the Eulerian–Lagrangian approach leveraged the inviscid solution obtained from panel codes to compute the forces acting on the particles (Hedde & Guffond 1995, Tran et al. 1995). In grid-based aerodynamic solutions, such as RANS simulation, the trajectories of the particles are tracked within the computational grid, and efficient algorithms to locate the particles in the mesh and to interpolate the flow variables to the particle positions must be deployed (Widhalm et al. 2008, Rendall & Allen 2014). The computation of the collection efficiency in the Eulerian–Lagrangian approach usually relies on a single front of particles, which is placed upstream of the impinged body in a region of nonperturbed flow and is tracked until particles impinge surfaces or are advected downstream. Common to the different Lagrangian approaches is the issue of particle resolution and injection location. A common strategy that was proven to be effective is to iteratively refine the seeding plane (Xie et al. 2020, Porter 2022, Bellosta et al. 2023).

A second modeling option is an Eulerian–Eulerian description that has been widely used to compute the dispersed phase via a two-fluid approach (see Bourgault et al. 1999, Iuliano et al. 2011, Jung & Myong 2013, Norde et al. 2017). The two-fluid approach treats the carrier and the dispersed phases as interpenetrating fluids (Balachandar & Eaton 2010). In the limit of one-way coupling, and when drag forces dominate the dispersed-phase dynamics, the equations describing the dynamics of a given particle size read

$$\begin{cases} \dfrac{\partial \alpha}{\partial t} + \nabla \cdot \left(\alpha \mathbf{v}_{\mathrm{p}}\right) = 0 \\ \dfrac{\partial \alpha \mathbf{v}_{\mathrm{p}}}{\partial t} + \nabla \cdot \left(\alpha \mathbf{v}_{\mathrm{p}} \otimes \mathbf{v}_{\mathrm{p}}\right) = \alpha f(\mathrm{Re}_{\mathrm{p}}, \mathrm{We}_{\mathrm{p}}) \dfrac{\left(\mathbf{v}_{\mathrm{f}} - \mathbf{v}_{\mathrm{p}}\right)}{\mathrm{St}}, \end{cases} \qquad 2.$$

where α is the volume fraction made nondimensional with its freestream value $\mathrm{LWC}/\rho_{\mathrm{p}}$. The advantages over the Lagrangian approach include lower computational times for 3D cases and the availability of a continuous description of the solution. Some difficulties arise in accounting for splashing droplets, shadow regions, and the impossibility of dealing with trajectory crossing. In Eulerian–Eulerian codes, the particle phase equations are solved numerically using either finite volume (Norde et al. 2017) or finite element discretizations (Bourgault et al. 1999). Shadow zones, which are regions of the computational domain that particles never reach due to finite Stokes number effects, introduce discontinuities in the solution. Shock-capturing finite volume schemes are particularly suited to solve the governing equations. Centered Jameson–Schmidt-Turkel-like schemes have been suggested with second- and fourth-order dissipation terms activated via a sensor based on the local particle volume fraction (Iuliano et al. 2011) or with local artificial dissipation (Tong & Luke 2005). Upwind schemes employing the solution of the Riemann problem to determine the numerical fluxes require additional attention due to the nonstrictly hyperbolic nature of the equations. Relaxation terms (Bellosta et al. 2023) or shallow-water-like pressure terms (Jung & Myong 2013) have been included to make the equations strictly hyperbolic.

Few approaches are available to track secondary droplets resulting from splashing or aerobreakup of larger droplets. Splashing particles reinjected into the volume have a different size distribution than the primary cloud, and their size depends on the splashing model employed, which is usually a function of the impingement angle and velocity. Therefore, each splashing event on the surface may release a different secondary particle size into the flowfield, thus increasing the computational effort since each particle size requires its own set of transport equations (Balachandar & Eaton 2010). The sidebar titled Polydispersed Particles describes how polydispersed particles are accounted for in icing simulations. Hospers (2013) suggested mapping the size probability distribution of splashing particles to a fixed number of bins to reduce the computational burden. Bellosta et al. (2023) presented a hybrid Eulerian–Lagrangian approach where the splashing particles coming from an Eulerian computation of the primary droplets are reinjected in the domain as Lagrangian particles.

2.3. Ice Accretion

The freezing of impinging water onto an accreted ice layer can be locally described as the moving-boundary phase change problem originally formulated by Stefan (1891). Liquid water and solid ice occupy adjacent regions that are in contact with a cold substrate and exposed to the surrounding

POLYDISPERSED PARTICLES

Current regulations provide different reference particle distributions for each icing regime. In simulations, the size probability distribution of the polydispersed phase is divided into a finite number of intervals, called bins. An Eulerian two-fluid description of the dispersed phase requires solving as many sets of equations as there are bins. Alternatively, if the governing equations are derived using the probability density function approach, one can handle polydispersity by including particle size as one of the phase space variables (Balachandar & Eaton 2010). This latter approach has yet to be applied in icing computations, since a few bins are usually enough to obtain accurate values for the collection efficiency. Although the Lagrangian approach allows for the direct tracking of a polydispersed cloud, the effects of polydispersity are routinely computed as a weighted sum of monodispersed computations. Zabaleta et al. (2024b) report a speedup in statistical convergence for a Lagrangian computation of the collection efficiency when tracking separate monodispersed clouds compared to tracking polydispersed particles. In Lagrangian simulation, computational time is generally directly proportional to the particle size of each bin, as the computational cost is related to the impinged surface area, which increases with the particles' Stokes number. In contrast, the computational cost for the Eulerian description is roughly independent of particle size (Bellosta et al. 2023).

air, as depicted in **Figure 2**. The location of the ice–water boundary moves over time due to ice accretion. Most numerical icing models discretize the surface of the aircraft to solve a 1D (in the normal direction) phase-change problem over time for each surface element. The 1D Stefan problem is a set of four equations describing the evolution of a single-component two-phase system as follows:

$$\begin{cases} \dfrac{\partial T_\mathrm{i}}{\partial t} = \alpha_\mathrm{i} \dfrac{\partial^2 T_\mathrm{i}}{\partial z^2} \\ \dfrac{\partial T_\mathrm{w}}{\partial t} = \alpha_\mathrm{w} \dfrac{\partial^2 T_\mathrm{w}}{\partial z^2} \\ \rho_\mathrm{i} \dfrac{\partial B}{\partial t} + \rho_\mathrm{w} \dfrac{\partial h}{\partial t} = \sum \dot{m} \\ \mathcal{L}_\mathrm{f} \rho_\mathrm{i} \dfrac{\partial B}{\partial t} = k_\mathrm{i} \left(\dfrac{\partial T_\mathrm{i}}{\partial z} \right)_{B^-} - k_\mathrm{w} \left(\dfrac{\partial T_\mathrm{w}}{\partial z} \right)_{B^+} \end{cases}, \tag{3}$$

where α is the heat diffusion coefficient, k is the thermal conductivity, $\mathcal{L}_\mathrm{f}$ is the latent heat of fusion, and variable z is the coordinate in the wall-normal direction. The first and second lines in Equation 3 describe the heat diffusion within the ice and water layers. The third line enforces mass conservation in the control volume. The mass fluxes on the right-hand side include the incoming mass due to impinging droplets, the mass lost due to evaporation and sublimation, and the mass fluxes entering the volume due to the presence of the liquid film. The last line is the Stefan condition, which enforces the equality of latent heat due to phase change to the net heat flux toward the upper and lower layers. Analytical solutions to the Stefan problem are available for an infinite or semi-infinite domain in the z direction (Huerre et al. 2025).

Messinger (1953) presented the first application of the Stefan problem to in-flight icing by introducing some simplifying assumptions. By assuming steady conditions, assuming uniform temperature on the substrate and in the liquid film, and neglecting heat conduction in the ice layer, the energy balance reads

$$\dot{m}_\mathrm{in} + \dot{m}_\mathrm{imp} = \dot{m}_\mathrm{ice} + \dot{m}_\mathrm{es} + \dot{m}_\mathrm{out}, \tag{4}$$

$$\dot{Q}_\mathrm{conv} + \dot{Q}_\mathrm{imp} + \dot{Q}_\mathrm{es} + \dot{Q}_\mathrm{r} = \dot{Q}_\mathrm{kin} + \dot{Q}_\mathrm{aero} + \dot{Q}_\mathrm{ice} + \dot{Q}_\mathrm{in}. \tag{5}$$

The mass balance accounts for the mass flux of incoming water droplets $\dot{m}_{\mathrm{imp}}$, the incoming water film from the adjacent cells $\dot{m}_{\mathrm{in}}$, and the outflow mass rate of water toward adjacent cells $\dot{m}_{\mathrm{out}}$, freezing mass rate $\dot{m}_{\mathrm{ice}}$, and loss due to evaporation or sublimation $\dot{m}_{\mathrm{es}}$. The energy balance includes the cooling due to air convection $\dot{Q}_{\mathrm{conv}}$, impinging particles $\dot{Q}_{\mathrm{imp}}$, evaporation or sublimation $\dot{Q}_{\mathrm{es}}$, and radiation $\dot{Q}_{\mathrm{r}}$. It also considers the heating from kinetic energy of the droplets $\dot{Q}_{\mathrm{kin}}$, the aerodynamic heating $\dot{Q}_{\mathrm{aero}}$, the release of latent heat of freezing $\dot{Q}_{\mathrm{ice}}$, and heating from water inflow $\dot{Q}_{\mathrm{in}}$ (Özgen & Canibek 2009). The unknowns of the problem are the interface temperature (water–air for glaze icing or no icing and ice–air for rime icing), the freezing mass rate $\dot{m}_{\mathrm{ice}}$, and the outflowing mass $\dot{m}_{\mathrm{out}}$, commonly referred to as runback water. For glaze ice, the film is considered very thin, enabling it to be considered isothermal at the freezing temperature. Thus, the energy balance governs the freezing rate, while the mass balance determines $\dot{m}_{\mathrm{out}}$. In instances of rime ice, no water mass exits the computational volume, allowing the coupled system of balance equations to be solved for the freezing rate and the air–ice interface temperature. In the absence of icing, the model produces the liquid film temperature and $\dot{m}_{\mathrm{out}}$. In the Messinger model, the water film flows from the stagnation point toward the trailing edge, assuming a fixed direction for runback water. To extend the solution to more complex configurations where multiple stagnation points may exist, as it is the case of a complex ice shape with horns, Zhu et al. (2012) developed an iterative approach, where the Messinger model is solved iteratively for the runback water term $\dot{m}_{\mathrm{out}}$, which is allowed to flow to neighboring cells in the direction of the wall stress.

Messinger model: pioneer model for ice accretion; solves a mass and energy balance to determine the ice growth rate

Shallow water icing model (SWIM): based on a system of partial differential equations and on lubrication theory, assuming that air shear stress is the main driving force for the water film

Extended Messinger model: extension of the Messinger model based on the solution of a Stefan problem; the energy equation and mass balance are combined to provide a first-order nonlinear differential equation for the ice thickness, which is solved numerically

To apply the Messinger model to unsteady ice accretion problems, a system of two partial differential equations (PDEs) for mass and energy balance is written, namely,

$$\begin{cases} \rho_{\mathrm{w}}\left[\dfrac{\partial h}{\partial t}+\nabla\cdot(\bar{\mathbf{v}}_{\mathrm{f}}h)\right]=\dot{m}_{\mathrm{imp}}-\dot{m}_{\mathrm{ice}}-\dot{m}_{\mathrm{es}} \\ \rho_{\mathrm{w}}\left[\dfrac{\partial(hC_{\mathrm{w}}\tilde{T})}{\partial t}+\nabla\cdot\left(\bar{\mathbf{v}}_{\mathrm{f}}hC_{\mathrm{w}}\tilde{T}\right)\right] \\ \qquad =\left[C_{\mathrm{w}}\tilde{T}_{\mathrm{d}}+\frac{\|\mathbf{v}_{\mathrm{p}}\|^2}{2}\right]\dot{m}_{\mathrm{imp}}+(L_{\mathrm{f}}-C_{\mathrm{ice}}\tilde{T})\dot{m}_{\mathrm{ice}}-\dot{Q}_{\mathrm{es}}+\dot{Q}_{\mathrm{conv}}, \end{cases} \tag{6}$$

where h is the water film depth, ρ_{w} is the water density, $\bar{\mathbf{v}}_{\mathrm{f}}$ is the average film velocity across the water film height, $\tilde{T}_{\mathrm{d}}$ is the droplets' temperature in degrees Celsius, $\tilde{T}$ is the surface temperature in degrees Celsius of the water film or ice depending on the rime or glaze ice state, and C_{ice} is the specific heat of ice. The wall film is driven by the shear stresses of airflow, pressure gradients, and gravitational or rotational body forces, according to lubrication theory. Although based on lubrication theory for the liquid film motion, this model is commonly known as the shallow water icing model (SWIM) (Bourgault et al. 2000). The model solves for the ice thickness B, the film thickness h, and the surface temperature T. The system is closed with a set of compatibility conditions to make the problem well-posed (see Bourgault et al. 2000). Compared to the Messinger model, the SWIM allows for an unsteady formulation of the icing problem and yields a variable film thickness distribution on the surface.

The extended Messinger model introduced by Myers (2001) includes heat diffusion in the ice layer. Myers argued that ice accretion occurs more slowly than convection in the ice and water film layers. The ratio of the two timescales can be expressed as the Fourier number $\mathrm{Fo}=\frac{t_{\mathrm{ice}}\alpha_{\mathrm{i}}}{B^2}=\frac{\alpha_{\mathrm{i}}\rho_{\mathrm{i}}}{\beta \mathrm{LWC} V_{\infty} B}$. The condition $\mathrm{Fo}\gg 1$ must hold for assuming scale separation, and it occurs if $B\ll 10^{-2}$ m. For thin ice and film layers, heat problems reduce to the steady heat diffusion equation, leading to linear temperature profiles. Additionally, the characteristic film thickness $\mathcal{O}(10^{-4})$ in icing is small enough that conduction through the water can be neglected. This is equivalent to assuming infinite conduction through the water, which allows the water to remain approximately at the freezing temperature. This enables the imposition of the boundary condition at the film–air interface directly at $z = B$, allowing the approximated Stefan problem for a given temperature at $z = 0$ to be solved by using the steady heat problem in the ice layer along with the Stefan condition.

The hypothesis of the Myers model fails when B is large and hence the characteristic time of ice growth is comparable to that of heat conduction in the ice layer. Gori et al. (2018) extended the model of Myers by incorporating the unsteady heat equation in the ice layer, resulting in an exact solution to the Stefan problem for a substrate with a fixed temperature and an infinitesimally small water film (Roisman 2010, Huerre et al. 2025). Recently, more complex Stefan problems that include additional water layers have been utilized to develop models for de-icing events (Chauvin et al. 2018, Gallia et al. 2023b) and ice crystal icing (Peters et al. 2024).

Liquid film and rivulets: after impinging, droplets possibly merge to create a thin continuous film that flows downstream, driven by pressure and shear forces from external airflow; a critical thickness can be eventually reached downstream where the film breaks into rivulets

2.3.1. Stochastic approach. Stochastic approaches to icing aim at computing the ice accumulation on surfaces by mimicking the random impact of water droplets and their subsequent freezing on a surface or an already accreted ice layer. The original idea, pioneered by Lozowski et al. (1983) and Prodi et al. (1994), was extended by Szilder & Lozowski (2005) to predict ice accretion on airfoils in the rime and glaze regime. Their novel approach, termed morphogenetic, combines a ballistic model for the particles' impact on the surface with a random walk model over the surface. At each step in the random walk process, a random number is generated and compared to the local freezing probability, defined as the local freezing fraction computed with the underlying icing model, e.g., the Messinger model, to determine the freezing location (Szilder & Lozowski 2018, Forsyth & Szilder 2023). Papillon Laroche et al. (2023) introduced an alternative stochastic model resorting to a surface grid instead of a volumetric lattice, which enables 2D computations on unstructured grids. Bellosta et al. (2024a) presented multistep morphogenetic simulations on arbitrary 3D geometries.

2.3.2. Liquid film dynamics. When impinging supercooled droplets do not freeze immediately upon impact with the surface, possibly due to the action of a thermal IPS, they tend to form static beads. Beads are possibly advected downstream due to the action of shear forces. Over time, these beads either merge into a continuous liquid film or form rivulets (Rothmayer & Tsao 2001), influenced by shear stress, pressure gradients, centrifugal forces, and droplet momentum (Silva et al. 2006). The resulting water film on the surface can be described, in general, using the incompressible Navier–Stokes equations, assuming constant density and viscosity. For the problem at hand, the film aspect ratio, defined as $\epsilon = \frac{h}{L}$ (with h denoting the height of the liquid film thickness and L representing the characteristic length in the flow direction) is very small, $\epsilon \ll 1$. Furthermore, a low-Re regime can be assumed for the film flow $\mathrm{Re} = \mathcal{O}(1)$; hence we find $\mathrm{Re}\frac{h}{L} \ll 1$. Given these assumptions, the governing equations are further simplified using lubrication theory, yielding a scalar, nonlinear advection–diffusion equation that describes the evolution of the water film depth h, namely, the first line in Equation 6. As reported by Myers & Hammond (1999) and Mu et al. (2017), the average film velocity, which encapsulates the effects of shear forces $\boldsymbol{\tau}$, pressure P gradients, and—when applicable—the centrifugal, Coriolis, and gravitational forces $\mathbf{a}$ (especially relevant in the icing of rotating components), is given by

$$\bar{\mathbf{v}}_\mathrm{f} = \frac{h}{2\mu_\mathrm{w}}\boldsymbol{\tau} - \frac{h^2}{3\mu_\mathrm{w}}\nabla P - \frac{h^2}{3\mu_\mathrm{w}}\rho_\mathrm{w}\mathbf{a}, \qquad 7.$$

where ρ_w and μ_w are the density and dynamic viscosity of water. Centrifugal and Coriolis forces affect the dynamics of the disperse phase and of the liquid film, as discussed in the sidebar titled Icing on Rotating Components. Most current icing simulation codes use this lubrication-theory framework to model the dynamics of the liquid film (Chauvin et al. 2018). While this formulation reliably predicts the behavior of the continuous film at the leading edge, it does not adequately capture the formation of rivulets in the runback region or the microphysical behavior of the

ICING ON ROTATING COMPONENTS

In-flight icing simulation tools that rely on the quasi-steady paradigm generally fail in accurately predicting ice accumulation on rotating components such as helicopter rotors, propellers, engine fans, open rotors, and wind turbines. An unsteady Eulerian approach allows for the computation of collection efficiency (Fouladi et al. 2015, Min & Yee 2023). In Lagrangian simulations, the time-averaged value of β can be obtained with a statistical approach by the injection of randomly placed particles (Baldan et al. 2023, Zabaleta et al. 2024b) or by defining multiple cloud fronts (Morelli et al. 2020). Additionally, centrifugal force impacts the dynamics of the water film. Various strategies have been proposed in recent years, moving from early 2D methodologies (Britton 1992) to hybrid 2D/3D methods (Bain et al. 2011, Kelly et al. 2018) and fully 3D approaches (Aliaga et al. 2011, Morelli et al. 2023, Caccia et al. 2024). In hybrid 2D/3D methods, a 3D flow analysis is loosely coupled to the icing module to predict a series of 2D ice shapes, or the 2D solutions of the aerodynamic flow field and droplet dynamics are interpolated over the blade surface. Kelly et al. (2018) calculated a trimmed flight condition using a multibody approach for rotor dynamics to determine the angle of attack and incident velocity. Habashi (2024, part V) reviewed rotor simulation methods that address rotor aerodynamics and icing solvers, including shedding, shed-ice tracking, and iced rotor dynamics.

dynamics and freezing of beads that form upon droplet impingement on the surface. An alternative approach to modeling the liquid phase dynamics on the surface explicitly incorporates the discrete formation and coalescence of beads. In this treatment, the dynamics of the liquid layer are described using a beading model (Ozcer et al. 2011). Upon impact, droplets form individual beads that coalesce with new incoming droplets until a critical thickness is reached, beyond which the forces from the external airflow and gravity overcome the liquid's surface tension. Depending on the water content on the surface, this leads either to the formation of rivulets or to the development of a continuous film, which is then treated using one of the models described in Section 2.3 for freezing. Other models describing rivulet formation typically rely on minimum total energy criteria, as proposed by Mikielewicz & Moszynski (1975) and later by Al-Khalil et al. (1994).

2.3.3. Density modeling. Once the ice mass accreted on the surface is determined by the thermodynamic solver, the actual displacement to retrieve the new geometry depends on the ice density value. In a multistep loop, due to the complex interaction of aerodynamics, particle impingement, and ice growth, different ice density models can lead to very different ice shapes. There are two distinct types of densities associated with in-flight icing: bulk density and void density. Vargas et al. (2007) measured bulk densities over a straight NACA 0012 airfoil in the glaze, mixed, and rime regimes, with values close to 917 kg/m^3. Void densities accounting for bubbles or air pockets trapped in the ice were measured to be close to 880 kg/m^3. Ice accretion on swept wings poses significant challenges for the modeling community, primarily due to ice scallops, also known as lobster tails, which are shallow, periodic grooves or ridges aligned with the local airflow direction, leading to large changes in void ice density (Vargas 2007, Bidwell 2014). Several empirical correlations have been proposed for ice density (Macklin 1962, Makkonen & Stallbrass 1984, Jones 1990). No void density models are necessary for morphogenetic simulations, and local density is a direct output of the model; however, its value depends on numerical model parameters.

Bulk density: the local ice density, which may vary because of trapped air or voids

Void density: the average density of ice, considering complex features such as feathers and lobster tails typical of three-dimensional ice shapes; it is calculated by dividing the predicted ice mass by the volume enclosed by the outer mold lines

2.3.4. Ice-induced roughness. During the initial phase of ice accretion, supercooled droplets impinge on the surface, coalescing into beads that partially or fully freeze, producing a rough surface. Unfrozen beads can run off as rivulets, freeze downstream, and build the rough, feather-like morphology typical of glaze ice, as illustrated in **Figure 3** (Fortin et al. 2004). These small-scale ice features caused by bead freezing and movement, known as ice roughness, play a crucial role in evaluating aerodynamic performances and convective heat transfer at the surface. The latter significantly influences the growth rate of glaze ice (Beaugendre et al. 2003b), making the inclusion of ice roughness effects extremely important. Ideally, accounting for the effects of these features would require solving the detailed geometry and the complete Navier–Stokes equations to capture all turbulence scales that can enhance heat transfer and fluid flow, a strategy that is computationally prohibitive on realistic geometries. Additionally, current icing models are not able to predict ice shapes at their roughness scales, and empirical modeling is used instead. The most viable solution is to approximate the roughness distribution with an equivalent sand grain roughness height, k_s. Although these models are commonly employed in thermo-aerodynamic calculations for both RANS (Aupoix 2015) and integral boundary layer methods (Radenac et al. 2018), the determination of the k_s value remains largely empirical. Experiments (McClain et al. 2017, Sotomayor-Zakharov et al. 2024) indicate that roughness is nonuniform across the ice surface and evolves over time. Following this, Yan et al. (2011) and Ignatowicz et al. (2023) developed empirical formulations for k_s where the parameter calibration is performed indirectly by comparing numerical ice shapes with experimental ones. As an alternative, Ozcer et al. (2011) proposed the beading model, already introduced for liquid film dynamics in Section 2.3.2, that aims to resemble the microphysical process, where the height of the frozen beads is used as the k_s value in the aerodynamic calculation.

Equivalent sand grain roughness height, k_s: represents a height for irregular and nonuniform rough surfaces, yielding results comparable to the uniform sand grain of Nikuradse in a fully rough flow regime

Runback ice: in running wet anti-ice mode, the liquid film may freeze upon reaching the unprotected areas, resulting in ridges that at certain locations could lead to significant aerodynamic penalties

2.4. Ice Shedding

Nonrotating components experience shedding due to aerodynamic forces that overcome adhesive and cohesive forces, often aided by activating a mechanical or thermal IPS, which breaks the ice volume and reduces adhesion between the ice and the surface (Zhang et al. 2012, Bennani et al. 2016, Marbœuf et al. 2020, Rausa et al. 2023). On rotating components, centrifugal acceleration generally drives crack initiation and delamination at the ice–substrate interface (Brouwers et al. 2010, Chen & Fu 2015, Anthony & Habashi 2021). Experimental data on the mechanical properties of ice needed to build the structural model for shedding analyses are scarce, with property dispersion and methodological constraints predominantly relying on freezer ice, despite noted differences in mechanical properties between impact and freezer ice. The former forms rapidly, is more heterogeneous, and typically shows lower strength and stiffness. In contrast, freezer ice forms slowly under controlled laboratory conditions, exhibiting greater uniformity and strength (Gammon et al. 1983, Mohamed & Farzaneh 2011, Fortin & Perron 2012).

2.5. Icing on Heated Surfaces

Ice accretion on a heated surface is of particular interest for the simulation of a thermal IPS. To account for the heating produced by these types of systems, the models presented in Section 2.3 are modified to account for heat transfer from the substratum to the ice or impinging water (da Silva et al. 2007, Reid et al. 2012, Chauvin et al. 2018, Gallia et al. 2023b). Thermal IPSs can operate in both de-icing and anti-icing mode; in particular, anti-icing operation can be divided into two further modes, as shown in **Figure 4**: the fully evaporative mode, where the impinging water evaporates before reaching the end of the protected area, and the running wet mode, which occurs when water flows beyond the protected region and freezes, creating runback ice. The operation mode determines the type of heat transfer that occurs at the interface. The heat flux from the wall can be written as

$$\dot{Q}_{\text{IPS}} = h_{\text{wall}} \left(T_{\text{wall}} - T \right), \qquad 8.$$

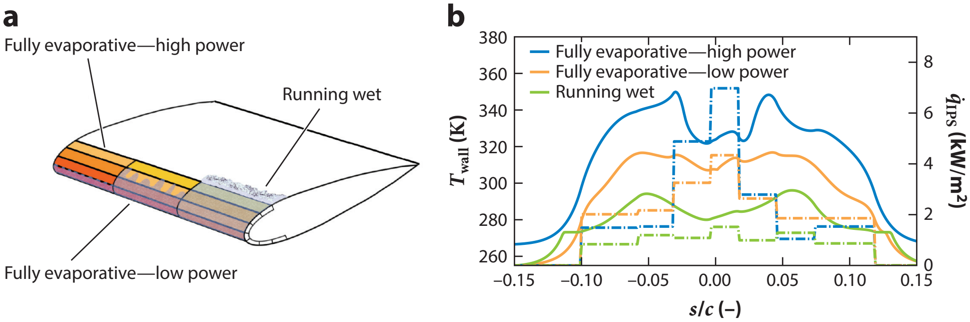

Figure 4

Illustration of the electrothermal ice protection system (IPS) anti-icing operational modes: fully evaporative and running wet. (*a*) Depiction of operational modes on a straight wing. (*b*) Distribution of surface temperature (*continuous lines*) and IPS power density (*dashed lines*) along the curvilinear abscissa for various operational modes.

where T_{wall} is the surface temperature of the substrate, T is the temperature of the phase in contact with the substrate (air, water, or ice), and h_{wall} is the appropriate HTC, convective when the wall sees airflow or running film, conductive when covered by static ice or water from melted ice.

In practice, the heat flux is introduced in different ways depending on the baseline ice accretion model used. For the Messinger or SWIM-based ice accretion models, this term is introduced as a volumetric heat source term in the energy balance. For models solving the heat conduction problem within the ice layer (Myers 2001), the heat flux is imposed as a boundary condition at the interface with the wall. Determining T_{wall} in Equation 8 requires modeling the heating mechanism of the IPS. For in-flight icing applications, two methods are commonly used: heating pads (i.e., electrothermal IPS) or hot air extracted from the aircraft engine (i.e., thermopneumatic IPS). In the former, only conduction in the substratum where the heating elements are placed needs to be modeled. This can be done by following two approaches. A simplified 1D lumped model uses an effective thermal conductivity and ignores temperature gradients through the ice layer (da Silva et al. 2007, Gutiérrez et al. 2021). Alternatively, the substrate may be treated as a multilayer solid, with full resolution of heat conduction in the direction normal and parallel to the surface (Reid et al. 2012, Bennani et al. 2020). In practice, both treatments yield very similar predictions of ice growth and evaporation, confirming that the principal thermal resistance resides not within the deep substrate but in the adjacent ice or liquid film. By contrast, thermopneumatic IPS—where hot bleed air from the engine warms the surface—demands a slightly more complex, partitioned, multiphysics coupling. The internal duct flow of hot air can be modeled using the RANS equations, the solid wall conduction is handled by a dedicated heat-transfer solver, and the external icing environment (droplet impingement plus liquid film flow) is treated as for the electrothermal IPS. The three solvers exchange wall temperature and heat flux boundary conditions and iterate until the temperature field and heat fluxes are self-consistent (Pellissier et al. 2011).

2.6. Geometry Updating

In the geometry update step, the initial aerodynamic surface is modified to include the newly accreted ice, producing an updated shape that reflects the ice buildup. This is necessary for both multistep and single-step methods to carry out the next accretion step and evaluate the aerodynamic penalties at the end of the process, as depicted in **Figure 5**. The updating procedure involves two distinct processes: updates of the surface geometry and updates of the volume geometry. Generally,

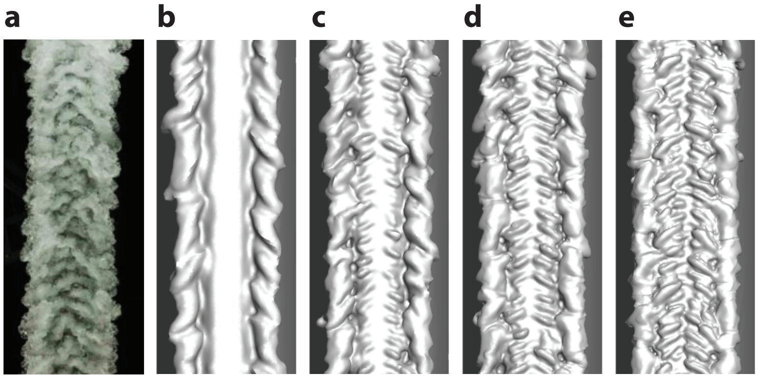

Figure 5

(*a*) Experimental ice shape reproduced from Bidwell (2014) (public domain). (*b–e*) Numerical ice shapes with a surface mesh size of 2 mm, 1.3 mm, 1 mm, and 0.7 mm, respectively. For reference, the chord length is 0.9144 m. Data provided by Ansys (Ozcer et al. 2022).

mesh morphing preserves the original grid topology and is typically faster than remeshing. However, its applicability is limited to small accretion times and simple glaze and rime shapes (Pendenza et al. 2015, Morelli et al. 2021). Embedded grid techniques, such as the IBM, can be used to prevent or, at the very least, substantially decrease the number of remeshing steps in a multistep simulation (Capizzano 2018, De Rosa et al. 2023, Paz et al. 2024). Both algebraic methods and PDE methods have been successfully applied to grid-based methods on structured (Hasanzadeh et al. 2015) and unstructured grids (Pueyo 2013, Pendenza et al. 2015). However, these methods may result in intersections or nonphysical regions in the updated geometry when dealing with concave regions or complex geometries, such as ice shapes. Ozcer et al. (2019) proposed an automated surface mesh projection scheme that wraps a new surface mesh over holes and crevices that are smaller than the minimum mesh spacing specification. The iced surface can also be described using a level-set method. Pena et al. (2016) and Lavoie et al. (2022) solved the level-set equation through a PDE-based approach, where the thermodynamic solver provides the icing velocity on the body surface. Paz et al. (2024) suggested tracking the surface in a Lagrangian manner using several subiterations, with the normal vector inferred from the level-set field. The level-set approach was also combined with implicit domain meshing techniques in a hybrid method, defining the level-set function using a signed-distance approach (Donizetti et al. 2023) or employing the Lagrangian displacement as a target (Bellosta et al. 2024a, Donizetti et al. 2024b). This enables the retrieval of a body-fitted representation of the iced surface, preventing potential mesh intersections due to the intrinsic properties of the level-set function. A well-known issue for the algebraic and PDE-based approaches is the conservation of the ice mass when prescribing the ice thickness displacement (Bourgault-Côté et al. 2017, Lavoie et al. 2022, Donizetti et al. 2023), particularly when dealing with concave and convex geometries. Solving iteratively by evolving the geometry in substeps improves ice mass conservation. The morphogenetic approach conserves the mass by construction. More details on the geometry update step can be found in the **Supplemental Appendix**.

Supplemental Material >

3. VALIDATION OF ICING SIMULATION TOOLS

Airframe, engine, and system manufacturers must demonstrate safe operation under icing conditions to comply with certification rules. Certification authorities typically require wind tunnel tests and flight tests in icing conditions or with artificial ice shapes. Due to a lack of fully validated simulation tools and the high costs of experimental tests, designers often resort to a conservative approach based on well-established technical solutions with a proven record of successful certification (certification by similarity). Certification based on similarity to existing aircraft is not viable for innovative configurations like AUAM, UAVs, all-electric aircraft, and new ice protection or detection systems. If a sufficient level of confidence in simulation results is achieved and manufacturers, along with certification authorities, reach a consensus that simulations could serve as the sole means of compliance, then certification by simulation can become a viable path for certifying innovative future aerial vehicles.

Results presented during the AIAA Ice Prediction Workshops (IPWs) (Laurendeau et al. 2022, 2024) document the unprecedented research effort over the past 20 years aimed at developing new ice accretion models and advanced 3D ice accretion software, matched by a corresponding improvement in experimental facilities for validation (AC-9C Aircraft Icing Technology Committee 2018). Unfortunately, the current gap between numerical predictions and experimental data makes using numerical tools for compliance in the certification process challenging. This gap relates to the complexity of ice accretion and the lack of understanding of key fluid dynamics phenomena like SLD dynamics, heat transfer in the presence of liquid films, roughness-induced transition, liquid film dynamics, and ice properties, especially the ice density model. On the other hand, the large sensitivity to operating conditions and model uncertainties requires a shift in the verification and validation (V&V) paradigm, currently limited to comparing computed ice shapes with wind tunnel tests. Uncertainty in operating conditions and the stochastic nature of ice accretion complicate cross-facility (AC-9C Aircraft Icing Technology Committee 2018) and cross-code comparisons (Laurendeau et al. 2022, 2024) of experimental and numerical validation results. The community has yet to define the precise objective of validation clearly. Commenting on current validation approaches, Habashi (2024, chapter 30) argued that most legacy codes are calibrated rather than validated; namely, they are adjusted to fit specific experimental campaigns but may not accurately predict outcomes under different geometries or operating conditions. This observation is particularly compelling, considering that various parameters significantly affect the resulting ice shapes. For instance, factors such as roughness height, selected density models, and the void density of ice all have substantial impacts.

Certification by simulation: relies on models, including analyses based on ground testing (wind tunnel) and numerical methods (computational fluid dynamics), as means of compliance

Verification and validation (V&V): the verification of a computer code establishes whether the implementation of the model is correct; its validation determines if the computational simulation agrees with physical reality by comparing it to experimental results

Maximum combined cross section (MCCS): the outer boundary of the combined individual cross sections of the ice shapes

Minimum combined cross section (mCCS): the innermost region of the combined individual sections

3.1. Assessment of Current Validation Practices

Validation of legacy icing codes has historically relied on comparing predicted ice shapes to experimental data from hand tracings of 3D ice shapes (NATO Task Group AVT-006 2001). Recently, laser scanning techniques have enabled the extraction of full 3D geometries of experimental shapes (Lee et al. 2014), allowing the definition of additional quantities like maximum combined cross section (MCCS) and minimum combined cross section (mCCS). Current validation and code-to-code comparisons still use single tracings or combined cross sections, with minimal usage of other data like accreted ice mass. Furthermore, insufficient attention is put into intermediate steps of the icing calculation, such as the collection efficiency and convective heat transfer distribution, arguably due to the lack of experimental data and difficulty in measuring those quantities in an icing campaign.

Figure 6 shows code-to-code and experiment-to-experiment comparisons for two icing conditions. A close examination of the figure reveals shortcomings in current V&V practices for icing prediction codes. **Figure 6*a*** presents numerical results from participants in the first IPW for glaze accretion on a straight wing, using advanced multistep codes (Laurendeau et al. 2022). Predicted ice shapes differ significantly among various codes, reflecting different models or implementations, and even among different users of the same code. This highlights sensitivity to epistemic uncertainty and numerical errors in icing models, especially for multistep approaches. Small discrepancies at the beginning of computation, like early horn formation due to different

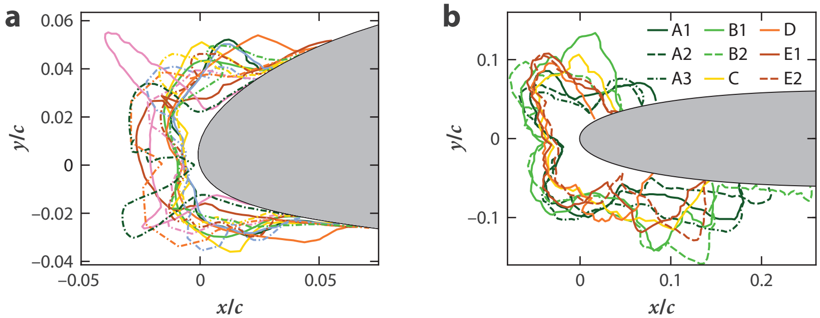

Figure 6

Code-to-code and experiment-to-experiment comparisons for glaze icing on straight wings. (*a*) Numerical results from different codes at the same nominal conditions. Data from Laurendeau et al. (2022). (*b*) Experimental repeatability from cross- and same-facility tests. Data from AC-9C Aircraft Icing Technology Committee (2018).

model parameters or surface discretizations, can greatly impact prediction accuracy in horn angle and position. An example is shown in **Figure 5**.

Figure 6*b* shows ice shape tracings under the same nominal conditions from different realizations within the same icing wind tunnel and across various facilities. Repeatability and reproducibility are low due to several factors. Icing tests are influenced by variability in critical parameters, such as LWC, droplet size distribution, and temperature, which are challenging to control. For instance, SAE standards for icing wind tunnel calibration (AC-9C Aircraft Icing Technology Committee 2025) allow up to 10% instrumentation uncertainty in critical cloud parameters and 20% spatial variability (Breitfuß et al. 2019). This variability can result in significant differences in repeated tests under the same conditions, both within and across facilities. In SLD conditions, aerothermal slips between droplets and the flow field influence ice accretion, as noted by Bora et al. (2023). The report from the AC-9C Aircraft Icing Technology Committee (2018) illustrates this variability through tests across different facilities. Spanwise variability in ice shapes exists, even on straight wings, with swept wings often rendering single tracings ineffective. MCCS or mCCS measures could improve the significance of these comparisons, although they are applicable only to simple geometries. Improvements in ice shape analysis are needed for assessing ice accretion on swept wings and complex geometries. Neubauer & Oztekin (2024) proposed a method for calculating ice shape metrics like MCCS and a general mean ice shape for any 3D geometry with twist, taper, and sweep. Time-resolved experimental scans (Neubauer et al. 2023) will enhance our understanding and validation of multistep methods.

3.2. Outlook on Validation Practices

While it is challenging, characterizing uncertainty in operating conditions during experimental campaigns is extremely valuable. Performing repeatability studies with different realizations under nominal conditions would allow for a fair comparison with numerical results. Numerical codes must consider operational and model uncertainties to evaluate their impact on predicted ice shape. Uncertainty quantification techniques propagate these uncertainties through a model, producing a probabilistic output validated against experimental data (Prince Raj et al. 2020, Gori et al. 2022, Gallia & Guardone 2024). **Figure 7** compares two experimental tracings of a rime ice shape on a NACA 0012 swept wing with numerical results from a model that accounted for uncertainties in operating conditions to compute icing probability at a specific spanwise section (Bellosta 2023).

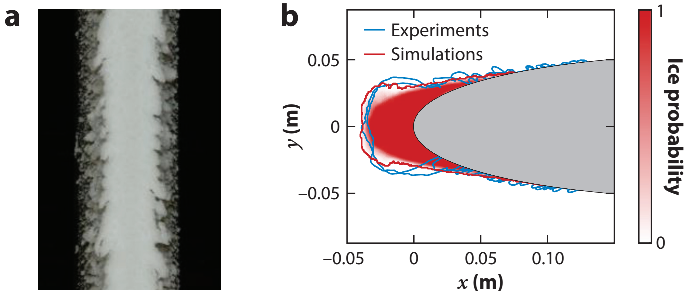

Figure 7

Validation of a numerical icing model considering aleatoric input uncertainties. (*a*) Experimental ice shape. Panel reproduced from Bidwell (2014) (public domain). (*b*) Ice probability from uncertainty quantification analysis. The two regions between the dark red area and the computed numerical maximum combined cross section correspond to low-density areas, marked as gray zones in the experimental ice shape. Panel reproduced from Bellosta (2023).

Moreover, the morphogenetic approach partly accounts for the stochastic nature of the ice accretion process through the random spatial initialization of the water particles and their sequential impact on the surface. The envelope of all realizations is close to the experimental tracings.

Validating aerodynamic performance on iced surfaces offers an interesting alternative to shape comparison, directly influencing aircraft handling in icing conditions. However, it may introduce significant model uncertainties, especially at higher angles of attack (De Gennaro et al. 2015). Limited experimental data mainly come from 3D-printed or cast ice shape replicas to examine performance degradation in wind tunnel tests (Broeren et al. 2018, 2020). Ozcer et al. (2023) showed that RANS closure models might need coefficient tuning to predict the aerodynamic response of laser-scanned ice shapes accurately. Numerical models usually produce smoother ice profiles than experiments. It is unclear if missing geometric features significantly impact aerodynamic penalties. Bornhoft et al. (2024b) performed WMLESs on a swept wing with laser-scanned and simplified ice shapes. They discovered that high-fidelity ice shapes enable precise load predictions, even with coarse grids, while simplified shapes require finer grids. Bellosta et al. (2024b) showed that geometric details of rime ice formations significantly impact predictions of straight-wing aerodynamics. Results in **Figure 8** reveal that the lift coefficient is highly sensitive to ice shape fidelity, with

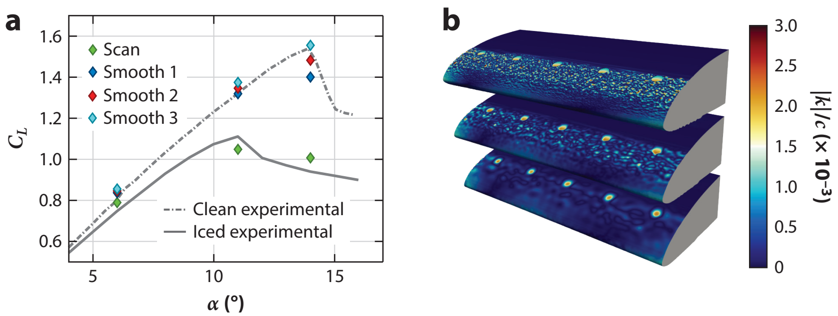

Figure 8

Wall-modeled large eddy simulation computation of airflow around a rime-iced NACA 0012 airfoil. The analysis considered increasingly detailed ice geometries, from smooth shapes to laser-scanned geometry. (*a*) Lift curve. (*b*) Roughness height *k* for three different levels of detail. Figure adapted from Bellosta et al. 2024b.

accurate predictions of experimental data possible only using laser-scanned geometry. To bridge the gap between experimental ice shapes and smoother simulated ones, adding sand-grain-type roughness may enhance aerodynamic predictions (Broeren et al. 2020). Stochastic ice accretion methods can be used to predict ice roughness (Gallia et al. 2023a).

SUMMARY POINTS

1. The numerical simulation of in-flight icing requires multidisciplinary modeling of the flow aerodynamics, the dynamics of the dispersed phase (supercooled droplets, ice crystals, snow), the film dynamics, and the ice accretion process. The results heavily depend on the underlying physical models, particularly the roughness, heat transfer, liquid film, and density models.
2. Particle dynamics modeling is satisfactory for small, spherical particles. Supercooled large droplet modeling, including aerobreakup and secondary droplets, requires further development. A tremendous research effort is underway to characterize the properties and dynamics of ice crystals. Research on snow is in its early stages.
3. Time-accurate ice accretion models (multistep method or fully unsteady) must be used to capture complex ice shapes such as horns, scallops, and feathers. Time-dependent, 4D, experimental results are needed for validating the simulation tools.
4. The ice accretion process is inherently stochastic. Therefore, deterministic models based on a limited number of experiments must be developed and used with caution, as should the comparison of experimental and simulation results.
5. The current best practices for code verification and validation are inadequate due to substantial variability in experimental references and uncertainties in wind tunnel conditions. Numerical results must consider the stochastic nature of the process, along with aleatoric and epistemic uncertainties. This principle also applies to interfacility and code-to-code comparisons. Furthermore, there are no established methods for comparing 3D shapes, such as those found on swept wings.

FUTURE ISSUES

1. Further experimental and numerical research activities are envisaged to improve the underlying physical models describing the ice accretion process, particularly concerning particle aerodynamics (supercooled large droplets, secondary droplets, ice crystals, snow), ice roughness, heat transfer, liquid film dynamics, rivulet formation, and density models.
2. Stochastic methods, such as the morphogenetic scheme, and uncertainty quantification techniques, should be refined and consistently applied to the verification and validation process. Experimentalists and simulation experts are encouraged to collaborate toward the definition of digital twins of icing wind tunnels accounting for operating uncertainty, such as the liquid water content distribution and the temperature and velocity slip of the injected particles.
3. Fundamental studies of the ice accretion process using direct numerical simulations or large eddy simulations of multiphase flow are within reach. They should be pursued

in the future to enhance our understanding of the ice accretion process and develop macroscopic models for the numerical simulation of the entire aircraft.

4. Future design and certification processes must take into account the uncertainty of operating conditions, physical models, and the nondeterministic nature of the ice accretion process from the earliest stages.
5. The use of simulation tools for assessing performance and handling quality degradation in icing conditions must be further investigated. The validation of icing experiments and simulations in terms of aerodynamic penalty should be combined with ice shape comparisons.

DISCLOSURE STATEMENT

The authors are not aware of any affiliations, memberships, funding, or financial holdings that might be perceived as affecting the objectivity of this review.

ACKNOWLEDGMENTS

The authors express their gratitude for the insightful comments and suggestions offered by Dr. Alberto Pueyo, Dr. Paolo Vanacore, Dr. Isik Ozcer, and Francesco Caccia.

LITERATURE CITED

AC-9C Aircraft Icing Technology Committee. 2018. Icing wind tunnel interfacility comparison tests. Tech. Pap. AIR5666A, SAE International

AC-9C Aircraft Icing Technology Committee. 2025. *Calibration and acceptance of icing wind tunnels*. Stand. ARP5905. SAE International

Aguilar B, Trontin P, Köbschall K, Dezitter F, Hussong J, Villedieu P. 2023. Experimental investigation and semi-empirical modeling of snowflake melting. *Int. J. Heat Mass Transf.* 209:124117

Al-Khalil KM, Keith TG Jr., De Witt KJ. 1994. Development of an improved model for runback water on aircraft surfaces. *J. Aircr.* 31:271–78

Aliaga CN, Aubè MS, Baruzzi GS, Habashi WG. 2011. FENSAP-ICE-Unsteady: unified in-flight icing simulation methodology for aircraft, rotorcraft, and jet engines. *J. Aircr.* 48:119–26

Anthony J, Habashi WG. 2021. Helicopter rotor ice shedding and trajectory analyses in forward flight. *J. Aircr.* 58:1051–67

Aupoix B. 2015. Improved heat transfer predictions on rough surfaces. *Int. J. Heat Fluid Flow* 56:160–71

Bae J, Yee K. 2022. Numerical investigation of droplet breakup effects on droplet–wall interactions under SLD conditions. *Int. J. Aeronaut. Space Sci.* 22:1005–18

Bain J, Deresz R, Sankar L, Egolf TA, Flemming R, Kreeger E. 2011. Effects of icing on rotary wing loads and surface heat transfer. In *49th AIAA Aerospace Sciences Meeting Including the New Horizons Forum and Aerospace Exposition*. AIAA

Balachandar S, Eaton JK. 2010. Turbulent dispersed multiphase flow. *Annu. Rev. Fluid Mech.* 42:111–33

Baldan G, Bellosta T, Guardone A. 2023. Efficient Lagrangian particle tracking algorithms for distributed-memory architectures. *Comput. Fluids* 256:105856

Beaugendre H, Morency F, Habashi WG. 2003a. FENSAP-ICE's three-dimensional in-flight ice accretion module: ICE3D. *J. Aircr.* 40:239–47

Beaugendre H, Morency F, Habashi WG, Benquet P. 2003b. Roughness implementation in FENSAP-ICE: model calibration and influence on ice shapes. *J. Aircr.* 40:1212–15

Bellosta T. 2023. *Numerical methods for 3D in-flight ice accretion under uncertainties*. PhD Diss., Politecnico di Milano

Bellosta T, Baldan G, Sirianni G, Guardone A. 2023. Lagrangian and Eulerian algorithms for water droplets in in-flight ice accretion. *J. Comput. Appl. Math.* 429:115230

Bellosta T, Donizetti A, Guardone A. 2024a. A multi-step stochastic approach to in-flight icing simulation. In *AIAA Aviation Forum and Ascend 2024*. AIAA

Bellosta T, Donizetti A, Zabaleta F, Bornhoft B, Jain S, et al. 2024b. Assessing relevant roughness scales for accurate prediction of iced airfoil aerodynamics. In *Proceedings of the Summer Program, Center for Turbulence Research*. Stanford University

Bennani L, Trontin P, Chauvin R, Villedieu P. 2020. A non-overlapping optimized Schwarz method for the heat equation with non linear boundary conditions and with applications to de-icing. *Comput. Math. Appl.* 80:1550–22

Bennani L, Villedieu P, Salaün M. 2016. A mixed adhesion–brittle fracture model and its application to the numerical study of ice shedding mechanisms. *Eng. Fract. Mech.* 158:59–80

Bhargava C, Loth E, Potapczuk M. 2005. Numerical simulation of icing clouds in the NASA Glenn Icing Research Tunnel. *J. Aircr.* 42:1442–51

Bidwell CS. 2014. Icing analysis of a swept NACA 0012 wing using LEWICE3D Version 3.48. In *6th AIAA Atmospheric and Space Environments Conference*. AIAA

Bocksell TL, Loth E. 2001. Random walk models for particle diffusion in free-shear flows. *AIAA J.* 39:1086–96

Bora VR, Gallia M, Knop I, Guardone A. 2023. Investigation of the influence of aero-thermal non-equilibrium conditions of an SLD cloud on airfoil icing. Tech. Pap. 2023-01-1406, SAE International

Bornhoft B, Jain SS, Goc K, Bose ST, Moin P. 2024a. Large-eddy simulations of the NACA23012 airfoil with laser-scanned ice shapes. *Aerosp. Sci. Technol.* 146:108957

Bornhoft BJ, Jain SS, Bose ST, Moin P. 2024b. Large-eddy simulations of the CRM65 swept wing under real and artificial icing conditions. In *AIAA SCITECH 2024 Forum*. AIAA

Bourgault Y, Beaugendre H, Habashi WG. 2000. Development of a shallow-water icing model in FENSAP-ICE. *J. Aircr.* 37:640–46

Bourgault Y, Habashi WG, Dompierre J, Baruzzi GS. 1999. A finite element method study of Eulerian droplets impingement models. *Int. J. Numer. Methods Fluids* 29:429–49

Bourgault-Côté S, Hasanzadeh K, Lavoie P, Laurendeau E. 2017. Multi-layer icing methodologies for conservative ice growth. In *7th European Conference for Aeronautics and Aerospace Sciences*. EUCASS

Brandt L, Coletti F. 2022. Particle-laden turbulence: progress and perspectives. *Annu. Rev. Fluid Mech.* 54:159–89

Breitfuß W, Wannemacher M, Knöbl F, Ferschitz H. 2019. Aerodynamic comparison of freezing rain and freezing drizzle conditions at the RTA icing wind tunnel. *SAE Int. J. Adv. Curr. Pract. Mobility* 2:245–55

Britton R. 1992. Development of an analytical method to predict helicopter main rotor performance in icing conditions. In *30th Aerospace Sciences Meeting and Exhibit*. AIAA

Broeren AP, Addy HE Jr., Lee S, Monastero MC, McClain ST. 2018. Three-dimensional ice-accretion measurement methodology for experimental aerodynamic simulation. *J. Aircr.* 55:817–28

Broeren AP, Lee S, Woodard BS, Bragg MB. 2020. Effect of geometric fidelity on the aerodynamics of a swept wing with glaze ice accretion. In *AIAA Aviation 2020 Forum*. AIAA

Brouwers EW, Palacios JL, Smith EC, Peterson AA. 2010. The experimental investigation of a rotor hover icing model with shedding. In *Annual Forum Proceedings - AHS International*, Vol. 2. American Helicopter Society

Budinger M, Pommier-Budinger V, Reysset A, Palanque V. 2021. Electromechanical resonant ice protection systems: energetic and power considerations. *AIAA J.* 59:2590–602

Caccia F, Abergo L, Guardone A. 2024. Towards blade-resolved ice accretion simulations of flexible blades using mixed-fidelity models. *J. Phys. Conf. Ser.* 2767:022046

Capizzano F. 2018. Automatic generation of locally refined Cartesian meshes: data management and algorithms. *Int. J. Numer. Methods Eng.* 113:789–813

Cebeci T, Kafyeke F. 2003. Aircraft icing. *Annu. Rev. Fluid Mech.* 35:11–21

Chauvin R, Bennani L, Trontin P, Villedieu P. 2018. An implicit time marching Galerkin method for the simulation of icing phenomena with a triple layer model. *Finite Elements Anal. Des.* 150:20–33

Chen Y, Fu L. 2015. Numerical simulation of helicopter blade ice shedding using a bilinear cohesive zone model. Tech. Pap. 2015-01-2121, SAE International

Cossali GE, Coghe A, Marengo M. 1997. The impact of a single drop on a wetted solid surface. *Exp. Fluids* 22:463–72

Costes M, Moens F. 2019. Advanced numerical prediction of iced airfoil aerodynamics. *Aerosp. Sci. Technol.* 91:186–207

da Silva GAL, Silvares OM, Zerbini EJGJ. 2007. Numerical simulation of airfoil thermal anti-ice operation, part 2: implementation and results. *J. Aircr.* 44:634–41

De Gennaro AM, Rowly CW, Martinelli L. 2015. Uncertainty quantification for airfoil icing using polynomial chaos expansions. *J. Aircr.* 52:1404–11

De Rosa D, Capizzano F, Cinquegrana D. 2023. Multi-step ice accretion by immersed boundaries. Tech. Pap. 2023-01-1484, SAE International

Donizetti A, Bellosta T, Guardone A. 2024a. Ice shape convergence in multistep ice accretion simulations. *J. Aircr.* 61:1761–74

Donizetti A, Bellosta T, Rausa A, Re B, Guardone A. 2023. Level-set mass-conservative front-tracking technique for multistep simulations of in-flight ice accretion. *J. Aircr.* 60:1050–60

Donizetti A, Bellosta T, Rausa A, Re B, Guardone A. 2024b. Three-dimensional front-tracking technique for multistep simulations of aircraft icing. *J. Aircr.* 62:328–40

Elghobashi S. 1994. On predicting particle-laden turbulent flows. *Appl. Sci. Res.* 52:309–29

Elghobashi S. 2019. Direct numerical simulation of turbulent flows laden with droplets or bubbles. *Annu. Rev. Fluid Mech.* 51:217–44

Ferschitz H, Wannemacher M, Bucek O, Knöbel F, Breitfuß W. 2017. Development of SLD capabilities in the RTA Icing Wind Tunnel. *SAE Int. J. Aerosp.* 10:12–21

Forsyth P, Szilder K. 2023. Experimental and numerical ice accretion shapes on a pitot probe model. In *International Conference on Icing of Aircraft, Engines, and Structures*. SAE International

Fortin G, Ilinca A, Laforte JL, Brandi V. 2004. New roughness computation method and geometric accretion model for airfoil icing. *J. Aircr.* 41:119–27

Fortin G, Perron J. 2012. Ice adhesion models to predict shear stress at shedding. *J. Adhes. Sci. Technol.* 26:523–53

Fouladi H, Aliaga CN, Habashi WG. 2015. Quasi-unsteady icing simulation of an oscillating airfoil. In *7th AIAA Atmospheric and Space Environments Conference*. AIAA

Gallia M, Bellosta T, Guardone A. 2023a. Automatic roughness characterization of simulated ice shapes. *J. Comput. Appl. Math.* 427:115114

Gallia M, Guardone A. 2024. Assessment of icing wind tunnel operational uncertainties on ice protection system performances. In *AIAA Aviation Forum and Ascend 2024*. AIAA

Gallia M, Rausa A, Martuffo A, Guardone A. 2023b. A comprehensive numerical model for numerical simulation of ice accretion and electro-thermal ice protection system in anti-icing and de-icing mode, with an ice shedding analysis. Tech. Pap. 2023-01-1463, SAE International

Gammon P, Kiefte H, Clouter M, Denner W. 1983. Elastic constants of artificial and natural ice samples by Brillouin spectroscopy. *J. Glaciol.* 29:433–60

Gori G, Congedo PM, Le Maître O, Bellosta T, Guardone A. 2022. Modeling in-flight ice accretion under uncertain conditions. *J. Aircr.* 59:799–813

Gori G, Parma G, Zocca M, Guardone A. 2018. Local solution to the unsteady Stefan problem for in-flight ice accretion modeling. *J. Aircr.* 55:251–62

Gutiérrez BA, Della Noce A, Gallia M, Bellosta T, Guardone A. 2021. Numerical simulation of a thermal ice protection system including state-of-the-art liquid film model. *J. Comput. Appl. Math.* 391:113454

Habashi WG, ed. 2024. *Handbook of Numerical Simulation of In-Flight Icing*. Springer International Publishing

Hasanzadeh K, Pena D, Hoarau Y, Laurendeau E. 2015. Multi-time step icing calculations using a 3D multi-block structured mesh generation procedure. Tech. Pap. 2015-01-2161, SAE International

Hedde T, Guffond D. 1995. ONERA three-dimensional icing model. *AIAA J.* 33:1038–45

Hess M, Koepke P, Schult I. 1998. Optical Properties of Aerosols and Clouds: the software package OPAC. *Bull. Am. Meteorol. Soc.* 79:831–44

Honsek R, Habashi WG. 2006. FENSAP-ICE: Eulerian modeling of droplet impingement in the SLD regime of aircraft icing. In *44th AIAA Aerospace Sciences Meeting and Exhibit*. AIAA

Hospers J. 2013. *Eulerian method for super-cooled large-droplet ice-accretion on aircraft wings*. PhD Diss., University of Twente

Hu X, Agrawal R, Zabaleta F, Bornhoft B, Yang X. 2024. Flow over ice roughness: Part I. Roughness heterogeneity. In *Proceedings of the Summer Program*, *Center for Turbulence Research*. Stanford University

Huerre A, Josserand C, Séon T. 2025. Freezing and capillarity. *Annu. Rev. Fluid Mech.* 57:257–84

Ignatowicz K, Morency F, Beaugendre H. 2023. Data-driven roughness estimation for glaze ice accretion simulation. Tech. Pap. 2023-01-1449, SAE International

Iuliano E, Mingione G, Petrosino F, Hervy F. 2011. Eulerian modeling of large droplet physics toward realistic aircraft icing simulation. *J. Aircr.* 48:1621–32

Jones KF. 1990. The density of natural ice accretions related to nondimensional icing parameters. *Q. J. R. Meteorol. Soc.* 116:477–96

Jung SK, Myong RS. 2013. A second-order positivity-preserving finite volume upwind scheme for air-mixed droplet flow in atmospheric icing. *Comput. Fluids* 86:459–69

Kelly D, Habashi WG, Quaranta G, Masarati P, Fossati M. 2018. Ice accretion effects on helicopter rotor performance, via multibody and CFD approaches. *J. Aircr.* 55:1165–76

König B, Fares E, Broeren AP. 2015. Lattice-Boltzmann analysis of three-dimensional ice shapes on a NACA 23012 airfoil. In *SAE 2015 International Conference on Icing of Aircraft*, *Engines*, *and Structures*. SAE International

Kozomara D, Amon J, Puffing R, Neubauer T, Schweighart S, et al. 2023. Experimental investigation of UAS rotors and ice protection systems in Appendix C icing conditions. Tech. Pap. 2023-01-1380, SAE International

Laurendeau E, Blanchet M, Zayni MK, Hann R, Radenac E, et al. 2024. Summary from the 2nd AIAA Ice Prediction Workshop. In *AIAA Aviation Forum and Ascend 2024*. AIAA

Laurendeau E, Bourgault-Cote S, Ozcer IA, Hann R, Radenac E, Pueyo A. 2022. Summary from the 1st AIAA Ice Prediction Workshop. In *AIAA Aviation 2022 Forum*. AIAA

Lavoie P, Pena D, Hoarau Y, Laurendeau E. 2018. Comparison of thermodynamic models for ice accretion on airfoils. *Int. J. Numer. Methods Heat Fluid Flow* 28:1004–30

Lavoie P, Radenac E, Blanchard G, Laurendeau E, Villedieu P. 2022. Immersed boundary methodology for multistep ice accretion using a level set. *J. Aircr.* 59:912–26

Lee S, Broeren AP, Kreeger RE, Potapczuk M, Utt L. 2014. Implementation and validation of 3D ice accretion measurement methodology. In *6th AIAA Atmospheric and Space Environments Conference*. AIAA

Lee S, Loth E. 2008. Simulation of icing on a cascade of stator blades. *J. Propul. Power* 24:1309–16

Lozowski EP, Stallabrass JR, Hearty PF. 1983. The icing of an unheated, nonrotating cylinder. Part I: A simulation model. *J. Appl. Meteorol. Climatol.* 22:2053–62

Macklin WC. 1962. The density and structure of ice formed by accretion. *Q. J. R. Meteorol. Soc.* 88:30–50

Makkonen L, Stallbrass J. 1984. *Ice accretion on cylinders and wires*. Tech. Rep., National Research Council Canada

Marbœuf A, Bennani L, Budinger M, Pommier-Budinger V. 2020. Electromechanical resonant ice protection systems: numerical investigation through a phase-field mixed adhesive/brittle fracture model. *Eng. Fract. Mech.* 230:106926

Maxey MR, Riley JJ. 1983. Equation of motion for a small rigid sphere in a nonuniform flow. *Phys. Fluids* 26:883–89

McClain ST, Vargas MM, Tsao JC, Broeren AP, Lee S. 2017. Ice accretion roughness measurements and modeling. In *7th European Conference for Aeronautics and Space Sciences*. EUCASS

Messinger BL. 1953. Equilibrium temperature of an unheated icing surface as a function of air speed. *J. Aeronaut. Sci.* 20:29–42

Mikielewicz J, Moszynski JR. 1975. Breakdown of a shear driven liquid. *Prace Instytutu Maszyn Przeplywowych* 66:3–11

Min S, Yee K. 2023. Numerical investigation of the unsteady effect owing to oscillation on airfoil icing. *Int. J. Heat Mass Transf.* 203:123791

Mohamed A, Farzaneh M. 2011. An experimental study on the tensile properties of atmospheric ice. *Cold Regions Sci. Technol.* 68:91–98

Mohseni M, Amirfazli A. 2013. A novel electro-thermal anti-icing system for fiber-reinforced polymer composite airfoils. *Cold Regions Sci. Technol.* 87:47–58

Morelli M, Bellosta T, Guardone A. 2021. Efficient radial basis function mesh deformation methods for aircraft icing. *J. Comput. Appl. Math.* 392:113492

Morelli M, Hauth J, Guardone A, Huan X, Zhou BY. 2023. A rotorcraft in-flight ice detection framework using computational aeroacoustics and Bayesian neural networks. *Struct. Multidiscip. Optim.* 66:197

Morelli M, Zhou BY, Guardone A. 2020. Acoustic characterization of glaze and rime ice structures on an oscillating airfoil via fully unsteady simulations. *J. Am. Helicopter Soc.* 65:1–12

Mu Z, Lin G, Bai L, Shen X, Bu X. 2017. 3D numerical simulation of ice accretion on a rotating surface. *Int. J. Aeronaut. Space Sci.* 18:352–64

Mundo C, Sommerfeld M, Tropea C. 1995. Droplet-wall collisions: experimental studies of the deformation and breakup process. *Int. J. Multiphase Flow* 21:151–73

Myers TG. 2001. Extension to the Messinger model for aircraft icing. *AIAA J.* 39:211–18

Myers TG, Hammond DW. 1999. Ice and water film growth from incoming supercooled droplets. *Int. J. Heat Mass Transf.* 42:2233–42

NATO Task Group AVT-006. 2001. *Ice accretion simulation evaluation test.* RTO Tech. Rep. 38, NATO

Neubauer T, Kozomara D, Puffing R, Teufl L. 2023. Time resolved 3D scanning of ice geometries in a large climatic wind tunnel. *SAE Int. J. Adv. Curr. Pract. Mobility* 6:1333–46

Neubauer T, Oztekin E. 2024. Characterization of propeller icing from 3D laser scan data. In *AIAA Aviation Forum and Ascend 2024*. AIAA

Nezzar D, Rannou J, Villedieu P, Bennani L, Balland M, Vénuat C. 2024. Simulation of ice shedding from rotating parts using phase-field fracture and cohesive zone models. In *AIAA Aviation Forum and Ascend 2024*. AIAA

Norde E, van der Weide ET, Hoeijmakers HW. 2017. Eulerian method for ice crystal icing with application to particle trajectories and accretion on a three-element airfoil. In *9th AIAA Atmospheric and Space Environments Conference*. AIAA

Ozcer I, Pueyo A, Menter F, Hafid S, Yang H. 2023. Numerical study of iced swept-wing performance degradation using RANS. In *International Conference on Icing of Aircraft, Engines, and Structures*. SAE International

Ozcer I, Switchenko D, Baruzzi GS, Chen J. 2019. Multi-shot icing simulations with automatic re-meshing. Tech. Pap. 2019-01-1956, SAE International

Ozcer IA, Aliaga C, Pueyo A, Zhang Y, Fouladi H, et al. 2022. Ansys - Bombardier 1st ice prediction workshop results. In *AIAA Aviation 2022 Forum*. AIAA

Ozcer IA, Baruzzi GS, Reid T, Habashi WG, Fossati M, Croce G. 2011. FENSAP-ICE: numerical prediction of ice roughness evolution, and its effects on ice shapes. Tech. Pap. 2011-38-0024, SAE International

Özgen S, Canibek M. 2009. Ice accretion simulation on multi-element airfoils using extended Messinger model. *Heat Mass Transf.* 45:305–22

Papillon Laroche H, Radenac E, Laurendeau E. 2023. Stochastic ice accretion model using an unstructured advancing front technique. *Int. J. Multiphase Flow* 163:104420

Paz PE, Radenac E, Blanchard G, Péron S, Laurendeau E, Villedieu P. 2024. Immersed boundary methodology for 3D multi-step ice accretion simulations. In *AIAA Aviation Forum and Ascend 2024*. AIAA

Pellissier M, Habashi W, Pueyo A. 2011. Optimization via FENSAP-ICE of aircraft hot-air anti-icing systems. *J. Aircr.* 48:265–76

Pena D, Hoarau Y, Laurendeau E. 2016. A single step ice accretion model using level-set method. *J. Fluids Struct.* 65:278–94

Pendenza A, Habashi WG, Fossati M. 2015. A 3D mesh deformation technique for irregular in-flight ice accretion. *Int. J. Numer. Methods Fluids* 79:215–42

Penner DC, Housman JA, Stich GD, Sousa VC, Koch JR, Duensing J. 2024. Wall-modeled large-eddy simulations of a swept wing with leading-edge ice. In *AIAA Aviation Forum and Ascend 2024*. AIAA

Peters T, Shelton J, Tang H, Trinh PH. 2024. An enthalpy-based model for the physics of ice-crystal icing. *J. Fluid Mech.* 1001:A12

Porter CE. 2022. A comparison of trajectory refinement schemes for GlennICE. In *AIAA Aviation 2022 Forum*. AIAA

Prince Raj L, Yee K, Myong RS. 2020. Sensitivity of ice accretion and aerodynamic performance degradation to critical physical and modeling parameters affecting airfoil icing. *Aerosp. Sci. Technol.* 98:105659

Prodi F, Smargiassi E, Porcu F. 1994. Stochastic models of ice accretion. *Atmosp. Res.* 32:95–114

Pueyo A. 2013. Efficient 3D artificial ice shapes simulations with 2D ice accretion codes using a 3-level correction. Tech. Pap. 2013-01-2136, SAE International

Radenac E, Blanchard G, Renaud T, Duchayne Q. 2023. Workflow for predictor–corrector simulations of in-flight ice accretion, with applications on swept wings. *Eng. Comput.* 4:2307–30

Radenac E, Kontogiannis A, Bayeux C, Villedieu P. 2018. An extended rough-wall model for an integral boundary layer model intended for ice accretion calculations. In *Atmospheric and Space Environments Conference*. AIAA

Rausa A, Caccia F, Guardone A. 2023. Multi-physics simulations of ice shedding from wind turbines. Tech. Pap. 2023-01-1479, SAE International

Reid T, Baruzzi GS, Habashi WG. 2012. FENSAP-ICE: unsteady conjugate heat transfer simulation of electrothermal de-icing. *J. Aircr.* 49:1101–9

Rendall T, Allen C. 2014. Finite-volume droplet trajectories for icing simulation. *Int. J. Multiphase Flow* 58:185–94

Roisman IV. 2010. Fast forced liquid film spreading on a substrate: flow, heat transfer and phase transition. *J. Fluid Mech.* 656:189–204

Rosenfeld D, Lensky IM. 1998. Satellite-based insights into precipitation formation processes in continental and maritime convective clouds. *Bull. Am. Meteorol. Soc.* 79:2457–76

Rothmayer A, Tsao J. 2001. On the incipient motion of air driven water beads. In *39th Aerospace Sciences Meeting and Exhibit*. AIAA

Schiller L. 1933. A drag coefficient correlation. *Zeit. Ver. Deutsch. Ing.* 77:318–20

Silva G, Silvares O, Zerbini E. 2006. Water film breakdown and rivulets formation effects on thermal anti-ice operation simulation. In *9th AIAA/ASME Joint Thermophysics and Heat Transfer Conference*. AIAA

Sotomayor-Zakharov D, Gaudioso R, Gallia M. 2025. Embedded LES of a turbulent thermal boundary layer over ice roughness. *Comput. Fluids* 297:106652

Sotomayor-Zakharov D, Radenac E, Gallia M, Guardone A, Knop I. 2024. Statistical analysis of the surface roughness on aircraft icing. *J. Aircr.* 61:245–56

Stefan J. 1891. Über die Theorie der Eisbildung, insbesondere über die Eisbildung im Polarmeere. *Ann. Phys.* 278:269–86

Szilder K, Lozowski EP. 2005. Simulation of airfoil icing with a novel morphogenetic model. *J. Aerosp. Eng.* 18:102–10

Szilder K, Lozowski EP. 2018. Comparing experimental ice accretions on a swept wing with 3D morphogenetic simulations. *J. Aircr.* 55:2546–49

Tong X, Luke E. 2005. Eulerian simulations of icing collection efficiency using a singularity diffusion model. In *43rd AIAA Aerospace Sciences Meeting and Exhibit*. AIAA

Tran P, Brahimi MT, Paraschivoiu I, Pueyo A, Tezok F. 1995. Ice accretion on aircraft wings with thermodynamic effects. *J. Aircr.* 32:444–46

Trontin P, Villedieu P. 2017. Revisited model for supercooled large droplet impact onto a solid surface. *J. Aircr.* 54:1189–204

Trontin P, Villedieu P. 2018. A comprehensive accretion model for glaciated icing conditions. *Int. J. Multiphase Flow* 108:105–23

Vargas M. 2007. Current experimental basis for modeling ice accretions on swept wings. *J. Aircr.* 44:274–90

Vargas M, Broughton H, Sims JJ, Bleeze B, Gaines V. 2007. Local and total density measurements in ice shapes. *J. Aircr.* 44:780–89

Vargas M, Feo A. 2011. Deformation and breakup of water droplets near an airfoil leading edge. *J. Aircr.* 48:1749–65

Wessel RA, Righi J. 1988. Generalized correlations for inertial impaction of particles on a circular cylinder. *Aerosol Sci. Technol.* 9:29–60

Widhalm M, Ronzheimer A, Meyer J. 2008. Lagrangian particle tracking on large unstructured three-dimensional meshes. In *46th AIAA Aerospace Sciences Meeting and Exhibit*. AIAA

Wong ML, Ghate A, Kenway GK, Angel JB, Kiris CC. 2024. Immersed boundary wall-modelled large eddy simulations of straight wings with three-dimensional ice accretion. In *AIAA Aviation Forum and Ascend 2024*. AIAA

Wright W. 2006. Further refinement of the LEWICE SLD model. In *44th AIAA Aerospace Sciences Meeting and Exhibit*. AIAA

Wright W, Potapczuk M. 2004. Semi-empirical modelling of SLD physics. In *42nd AIAA Aerospace Sciences Meeting and Exhibit*. AIAA

Wright WB, Potapczuk MG, Levinson LH. 2008. Comparison of LEWICE and GlennICE in the SLD regime. In *46th AIAA Aerospace Sciences Meeting and Exhibit*. AIAA

Xie L, Li P, Chen H, Liu H. 2020. Robust and efficient prediction of the collection efficiency in icing accretion simulation for 3D complex geometries using the Lagrangian approach I: an adaptive interpolation method based on the restricted radial basis functions. *Int. J. Heat Mass Transf.* 150:119290

Yan L, Chao W, Shi-nan C, Du C. 2011. Simulation of ice accretion based on roughness distribution. *Procedia Eng.* 17:160–77

Yang X, McGilvray M, Gillespie D. 2023. Sticking–erosion model for ice crystal icing using particle size distribution. *AIAA J.* 61:4976–89

Yarin AL. 2006. Drop impact dynamics: splashing, spreading, receding, bouncing. *Annu. Rev. Fluid Mech.* 38:159–92

Zabaleta F, Bornhoft B, Jain SS, Bose ST, Moin P. 2024a. Large-eddy simulations of heat transfer from iced surfaces. In *Center for Turbulence Research Annual Research Briefs 2024*. Stanford University

Zabaleta F, Jain SS, Bornhoft BJ, Bose S, Moin P. 2024b. Large-eddy simulation of supercooled large droplets impingement using a Lagrangian particle approach. In *AIAA Aviation Forum and Ascend 2024*. AIAA

Zhang H, Guan B, Wei R, Bai B. 2025. Effect of the spray bar on gas–liquid two-phase flow characteristics in icing wind tunnel. *Appl. Thermal Eng.* 262:125303

Zhang S, El Kerdi O, Khurram RA, Habashi WG. 2012. FEM analysis of in-flight ice break-up. *Finite Elem. Anal. Des.* 57:55–66

Zhu CX, Fu B, Sun Z, Zhu CL. 2012. 3D ice accretion simulation for complex configuration basing on improved Messinger model. *Int. J. Mod. Phys. Conf. Ser.* 19:341–50